Mapping the brain-wide network effects by optogenetic activation of the corpus callosum

Yi Chen[1,2], Filip Sobczak[1,2], Patricia Pais-Roldán[1,2], Cornelius Schwarz[3], Alan P. Koretsky[4], Xin Yu[1, 5*]

1 Research Group of Translational Neuroimaging and Neural Control, High-field Magnetic Resonance, Max Planck Institute for Biological Cybernetics, Tübingen, Baden-Württemberg, Germany

2 Graduate Training Centre of Neuroscience, University of Tübingen, Tübingen, Baden-Württemberg, Germany

3 Werner Reichardt Center for Integrative Neuroscience, Tübingen, Baden-Württemberg, Germany

4 National Institute of Neurological Disorders and Stroke, Bethesda, Maryland, United States of America

5 Athinoula A. Martinos Center for Biomedical Imaging, Massachusetts General Hospital and Harvard Medical School, Charlestown, Massachusetts, United States of America

Corresponding author:

Dr. Xin Yu
Email: xin.yu@tuebingen.mpg.de
Address: Max-Planck-Ring 11, 72076, Tuebingen, Germany
Phone: +497071 601-740
Fax: +49 7071 601-701

This PDF file includes:

    Main Text
    Main Figures 1 to 4
    Supplementary Information

36 **ABSTRACT (179 words)**

37 The optogenetically driven manipulation of circuit-specific activity enabled functional causality studies in animals,

38 but its global effect on the brain is rarely reported. Here, we applied simultaneous fMRI with calcium recording to

39 map brain-wide activity by optogenetic activation of fibers running in one orientation along the corpus callosum(CC)

40 connecting the barrel cortex(BC). Robust positive BOLD signals were detected in the ipsilateral BC due to

41 antidromic activity, which spread to ipsilateral motor cortex(MC) and posterior thalamus(PO). In the orthodromic

42 target (contralateral barrel cortex), positive BOLD signals were reliably evoked by 2Hz light pulses, whereas 40Hz

43 light pulses led to a reversed sign of BOLD - indicative of CC-mediated inhibition. This presumed optogenetic CC-

44 mediated inhibition was further elucidated by pairing light with peripheral whisker stimulation at varied inter-

45 stimulus intervals. Whisker induced positive BOLD, and calcium signals were reduced at inter-stimulus intervals

46 of 50/100ms. The calcium-amplitude modulation (AM)-based correlation with whole-brain fMRI signal revealed

47 that the inhibitory effects spread to contralateral BC as well as ipsilateral MC and PO. This work raises the need of

48 fMRI to elucidate the brain-wide network activation in response to projection-specific optogenetic stimulation.

2

49   **INTRODUCTION**

50   The genetic expression of channelrhodopsin (ChR2) has been extensively applied to target specific cell types to

51   ensure the activation of neuronal ensembles of interest [1-4]. Optogenetic tools have revolutionized the strategy to

52   perturb or manipulate the behavior of animals [5-8]. To interpret the linkage of the brain function to specific

53   behavioral readout relies on the assumed circuit-specific manipulation through *in vivo* optogenetic activation [9-

54   12]. Optogenetic activation of numerous brain sites and defined neuronal populations in animals has been very

55   successful to modulate behavior. However, there is a lack of systematic mapping of the result of specific modulation

56   on brain-wide network activity, which may relay and affect the proposed link between function and behavior.

57   Progress in this direction depends on the combined application of methods to explore large scale brain dynamics as

58   well [13-16]. One useful method for this purpose is functional magnetic resonance imaging (fMRI) , which has

59   been successfully combined with optogenetics [17-22]. We use here a method that adds GCaMP-mediated calcium

60   recordings through an optical fiber for concurrent fMRI and neuronal calcium signal recording [23-27]. This multi-

61   modal cross-scale brain dynamic mapping scheme allows elucidating network activity upon circuit-specific

62   optogenetic activation on the specific target level as well as across large brain regions [19, 23-25, 27-29].

63   Corpus callosum (CC), the major neural fiber bundles connecting the two hemispheres, plays a critical role to

64   mediate the interhemispheric cortico-cortical connections [30-32]. Despite the highly-correlated structural

65   anomalies of the CC with a wide range of disorders, e.g., schizophrenia [33, 34], autism [35, 36], epilepsy [37, 38]

66   and mental retardation [39, 40], CC-mediated neural mechanisms are primarily studied in loss-of-function models,

67   such as split-brain/callosotomy or partial callosal lesion [31, 41, 42]. To directly investigate the functional roles of

68   callosal projections on regulating the interhemispheric excitatory-inhibitory balance, both *in vitro* and *in vivo* studies

69   have applied micro-stimulation on one hemisphere or the callosal fiber bundles [43-46], or performed bilateral

70   motor or sensory tasks in both human [47-50] and animal models [50-54]. Since the callosal fibers are reciprocally

71   projecting to two hemispheres, bilateral, ortho- vs. antidromically evoked neural activity has been difficult to

72   disentangle. With optogenetic tools, the callosal projection neurons can be specifically (primarily) labeled with

73   ChR2 from one hemisphere, enabling the unidirectional modulation of callosal activity [55-57]. The optogenetically

74   driven callosal activity has been particularly helpful to disentangle interhemispheric inhibitory effects, e.g., in the

75   auditory cortex [58], prefrontal cortex [59] or hindlimb somatosensory cortex [60]. The goal of the present studies

76   was to widen the view beyond of target–specific excitatory-inhibitory regulation by using multi-modal fMRI

77   platform to characterize the global neural network activity upon optogenetic callosal activation.

78   In the present study, we implemented the multi-modal fMRI platform with optogenetics to map the CC-mediated

79   inhibition on the brain-wide network dynamics in three consecutive steps. First, we identified the antidromic vs.

80   orthodromic effect of CC-specific optogenetic stimulation. Optogenetic stimulation of callosal fibers connecting

3

81 the barrel cortex (BC) to the other hemisphere, revealed robust antidromic activation in the ipsilateral BC. In the

82 orthodromic direction, both fMRI and neuronal calcium signals in the contralateral BC indicated strong depression

83 of calcium signals with 40Hz light pulses. Second, we specified the temporal characteristics of this presumptive

84 CC-mediated inhibition on the thalamocortical activation to the BC. The optogenetic CC light pulses were paired

85 with the whisker stimulation electrical pulses at varying intervals from 0 ms to 200 ms in a randomized stimulation

86 scheme. Significant inhibitory effects at 50 ms and 100 ms interval were detected by both fMRI and neural calcium

87 recordings of the right BC activated by whisker stimulation, but little difference was observed in the antidromically

88 evoked fMRI signal in the ipsilateral BC. Thirdly, to further examine the brain-wide activity regulation upon paired

89 optogenetic and whisker stimulation, the concurrent evoked-calcium signals in the contralateral BC was real-time

90 detected at varying conditions and correlated with whole-brain fMRI signals. Besides the contralateral BC, the

91 homologous ventral part of the ipsilateral BC, the motor cortex and posterior thalamus (PO) from the same side of

92 the contralateral BC were detected in the correlation maps, showing amplitude modulation by CC-mediated

93 inhibition at varied time intervals. This study not only specifies the optogenetically driven CC-mediated regulation

94 of the local excitation/inhibition balance but also depicts the power of multi-modal fMRI to characterize the brain-

95 wide network activity associated with circuit-specific optogenetic activations *in vivo*. It highlights a vital aspect of

96 the brain-wide activity for circuit-specific causality studies with optogenetic tools.

97 **RESULTS**

98 **Antidromic activation by callosal optogenetic stimulation.**

99 By injecting the AAV-ChR2 viral vectors into the barrel cortex (BC) of rats, ChR2 can be expressed in callosal

100 projection neurons (CPNs), in particular through their axonal fiber bundles projecting to the contralateral BC (**Fig.**

101 **1a)** [56, 61]. Based on our previous work [62], an MRI-guided robotic arm was used to provide high flexibility to

102 insert the optical fiber and sufficient targeting accuracy on the ~200 μm callosal fiber bundle for multi-modal fMRI.

103 The most salient BOLD fMRI signal evoked by CC optogenetic stimulation was detected at the ipsilateral BC

104 housing the labeled CPN (n = 8 animals, **Fig. 1b, c,** 5 Hz light pulses). The antidromically evoked hemodynamic

105 responses to 5 Hz stimulation were significantly stronger than the responses to 2 Hz (**Fig. 1d**). In addition,

106 antidromic BOLD and local field potential (LFP) signal were evoked by systematically varying laser power, light

107 pulse width, frequency and duration of the optogenetic stimulation (**Fig. 1e**, **Fig. S1** and **S2**). The fMRI analysis

108 revealed widespread brain activation in the ipsilateral hemisphere, which likely originates from antidromic CPN

109 activity spread by multi-synaptic pathways to the motor cortex and posterior thalamus (**Fig. 1f**). These widespread

110 ipsilateral effects were readily seen with 5Hz stimulation paradigm but could not be evoked using lower stimulus

111 frequencies.

4

112 Next, we examined the temporal characteristics of the antidromic activity. In general, CC-mediated antidromic LFP

113 responses in BC to different pulse widths and frequencies were similar to the responses observed when BC was

114 directly activated (**Fig. S3** and **S4**). Likewise, the whole-brain BOLD signal showed time courses and distributions

115 as reported earlier with direct BC stimulation [17, 63]. We were concerned that the stimulation light could have

116 activated CPN directly in the BC. To test this concern, we recorded the LFPs evoked by optogenetic CC and direct

117 BC stimulation in the same rat (**Fig. 1g, h**), and found that the latency of the response was systematically higher for

118 CC as compared to BC stimulation (negative peak latency: BC: 8.13 ± 1.89 ms, CC: 11.27 ± 0.78 ms; positive peak

119 latency: BC: 17.00 ± 4.65 ms, CC: 21.07 ± 2.60 ms; n = 6 animals, paired t test, *p = 0.002, **p = 0.009) (**Fig. 1i**).

120 Otherwise the time course of the LFP response was similar, which showed, firstly that CC stimulation is likely

121 stimulating the CC axons as intended, and secondly that BC is activated in a very similar way by CPNs as with

122 direct stimulation. In support of this conclusion, we found that optogenetically activating callosal fibers from the

123 other hemisphere (opposite to the virus injection site) readily showed latency differences (**Fig. S5),** as expected

124 from the axonal conduction delays of the transmission of the electrical impulses [64, 65].

125 **Orthodromic activation by callosal optogenetic stimulation.**

126 Compared to antidromically evoked activity, the BOLD signal in the contralateral hemisphere evoked by

127 orthodromic stimulation was smaller, and the stimulus-response relationship was different. For instance, quite

128 different from the antidromic situation, the BOLD signal observed with 2 Hz optogenetic CC stimulation was

129 stronger than that with 5 Hz (**Fig. S6**). To investigate the CC-mediated corticocortical interaction in the contralateral

130 hemisphere, we injected the Syn-GCaMP6f and CaMKII-ChR2-mCherry into the left and right BC, respectively,

131 and recorded both calcium and LFP signal upon optogenetic CC stimulation (**Fig. 2a, b**). Here we focused on layer

132 5 (**Fig. 2b**), because it is the main target lamina of corpus callosum projections [58, 66], as well as the main output

133 layer of the barrel cortex [67]. **Fig. 2c** shows the frequency-dependent orthodromic calcium signals from one

134 representative rat. As mentioned before evoked calcium transients appeared in strict frequency-dependent fashion.

135 A strong transient was detected following each light pulse at 2 Hz, while at higher frequencies, only the first pulse

136 triggered a full-fledged calcium response (**Fig. 2c**). The subsequent pulse responses were depressed or missing

137 entirely and gave way to a slow decrement in fluorescence (**Fig. 2c**). The decrement of Ca^{2+} signal was constantly

138 present throughout the entire stimulus interval (see gray bar 40 Hz stimulation in **Fig. 2c**), and slowly relaxed back

139 to baseline only after the end of stimulation. Simultaneous LFP and calcium recordings in a representative rat shared

140 the same pattern, strengthening the notion of a strong suppression of responses at higher stimulus frequencies (**Fig.**

141 **S7**), and offering an explanation for the likewise decreased orthodromic BOLD signals at 5 Hz (**Fig. S6**). The

142 calcium baseline drift for 40 Hz was reproduced in animals and was quantified in **Fig. 2d**, suggesting a highly robust

143 corticocortical inhibition effect as previously reported by electrophysiological recording [59, 68, 69]. The evoked

144 LFP and calcium signals dependencies on the laser power, light pulse width and duration provide strong evidence

145 for reliable detection of the orthodromic activity (**Fig. S8-10**). It is noteworthy that the CC-mediated orthodromic

146 activity shows different response patterns for both LFP/calcium and fMRI signals from the antidromic activity,

147 indicating a distinct impact on the local excitation-inhibition balance through the CC-mediated inputs.

148 **The CC-mediated inhibitory effects on the sensory-evoked cortical activity**

149 Next, we investigated the effect of CC-mediated suppression on sensory-evoked cortical activity. The optogenetic

150 light pulse train ('O', 2 Hz, 16 pulses in 8 s) for CC optogenetic stimulation was delivered at time intervals of 0,

151 50, 100 and 200ms after stimulating the primary afferents in the whisker pad with a microstimulation pulse train

152 ('W', 2 Hz, 16 pulses). In total 6 conditions (W, O, OW, O50W, O100W and O200W, OxW means optogenetic

153 pulse leads the whisker stimulation pulse for "x" ms) were delivered in trials of randomized order (**Fig. 3a**) using

154 the multi-model fMRI platform (**Fig. 3b**). Typical raw calcium signals and stimulation design are shown in **Fig. 3c**

155 with a W condition leading the other randomized 12 epochs (6 conditions repeated twice in a randomized order).

156 We found a strong suppression of BOLD in the orthodromic direction with latencies of 50 and 100 ms (**Fig. 3d, g**).

157 The suppression was partially recovered at the O200W condition. This phenomenon was absent on the antidromic

158 side (**Fig, 3g**). A similar picture emerged with averaged calcium signals recorded in layer 5 of the contralateral BC

159 (**Fig.3e**). Ca^{2+} signals and BOLD were highly correlated (**Fig.3g, e**), showing reduced calcium percentage changes

160 at O50W and O100W conditions across animals (**Fig.3f**). Normalizing both signals to the whisker-only (W)

161 condition (**Fig. S11**), we find the mean signal changes of BOLD from 100% (W) to 107.3%, 59.2%, 56.8% and

162 100.4%, while the calcium signal changed from 100% (W) to 127.8%, 45.2%, 59.5% and 107.1% at conditions of

163 OW, O50W, O100W, and O200W, respectively (**Fig.3h**). To investigate the temporal features of the interaction on

164 a more precise scale, we refined the stimulus intervals for whisker stimulation by adding 10 and 25 ms conditions

165 (W, OW, O10W, O25W, O50W, O100W, and O200W) in another group of rats (**Fig. 3i** and **Fig. S12**). Again

166 similar patterns emerged as seen before (**Fig. 3i** and **Fig. S12**). For O10W, no significant difference was observed

167 in comparison to the OW condition, but the calcium responses at O25W were significantly lower than the OW

168 condition (**Fig. S12**). As reported from *in vitro* CC electrical stimulation studies by Kawaguchi et al. [44], CC

169 stimulation leads to two inhibitory postsynaptic potential (IPSP) peaks (the earlier peak at ~30 ms, and the later

170 peak at ~180 ms), which could underlie the inhibitory effects at O25W and the later recovery at O200W to different

171 extents. Furthermore, the simultaneous LFP and calcium recording confirmed the time-interval specific inhibitory

172 effects by direct optogenetic CC stimulation to modulate the sensory-evoked cortical activity pattern in the BC (**Fig.**

173 **S13**). These results are consistent with results using whisker, forepaw, and visual stimulation in rodents and human

174 studies [47-54].

175 **Global network mapping based on the optogenetically-driven CC-mediated inhibitory effects**

6

176   The 3D fMRI data with concurrent calcium signal acquired at different conditions with CC and whisker stimulation

177   allowed analyzing the global effect of the optogenetically-driven CC-mediated inhibition. To this end, the calcium

178   signal amplitude modulation (AM) factor was applied to the ideal function produced by the general linear model

179   (GLM), which was correlated with the 3D fMRI time course (**Fig. S14**) [24, 70]. As shown in Fig S14, the calcium-

180   AM regressor is derived from the stimulation-driven ideal function, of which the GLM analysis leads to a AM-

181   specific correlation with the whole brain fMRI signal. Thus, the calcium-based AM-correlation with the entire brain

182   generated a map of global brain dynamic changes related to specific CC-mediated inhibition effect. The strongest

183   correlation was found in the left BC (**Fig 4**). A positive correlation was further observed in the ipsilateral motor

184   cortex and posterior thalamus (PO), which are projection targets of the BC, as well as the vental right BC (**Fig. 4a,**

185   **b, c**). We next extracted the time courses from the highlighted ROIs to examine the changes of the fMRI signals at

186   different conditions. The averaged time courses from the right BC ROI reflected the patterns seen in the

187   orthodromically affected BC before. In these conditions (O50W and O100W), the BOLD signals were reduced with

188   respect to the other conditions (**Fig. 4d**). Similar patterns of BOLD responses were detected in the MC (**Fig. 4e**) as

189   well as the PO (**Fig. 4f**) directly connected to the left BC. It is noteworthy that the positively correlated right BC

190   area was not overlapping with cortical areas housing the CPNs (**Fig. 3**). In summary, these results demonstrate that

191   the global network is modulated with the CC-specific evoked activity in BC. The specificity of CPN precludes the

192   possibility that MC and PO might have integrated the callosal and sensory input independently of BC.

193   **DISCUSSION**

194   We have performed simultaneous BOLD-fMRI and calcium recording in combination with callosal-circuit specific

195   optogenetic stimulation to map the brain-wide network activation. The robust BOLD signal due to the antidromic

196   activity was detected in the ipsilateral BC, which also led to fMRI detection in the ipsilateral MC and PO region

197   with the higher frequency stimulus. In contrast, the positive BOLD signal through the CC-orthodromic activity was

198   only reliably observed at the lower frequency optogenetic stimulus. With the 40Hz light pulses, the calcium baseline

199   suppression was detected and interpreted to be due to the CC-mediated cortico-cortical inhibitory effect. To further

200   test this CC-mediated inhibition was further paired with the whisker stimulation paradigm at varying inter-stimulus

201   intervals from 0 ms to 200 ms, showing significant suppression at the O50W and O100W conditions in the left BC

202   by the concurrent fMRI and calcium recording. By extracting the event-dependent calcium peak amplitudes at

203   varied conditions as a regressor, an amplitude modulation (AM)-based correlation map revealed the brain-wide

204   inhibitory effects spreading through the ventral border of the right BC and the left MC and PO. Thus, the multi-

205   modal fMRI platform provides a thorough brain-wide network activation maps for the CC-specific optogenetic

206   stimulation.

207   The observation of strong antidromic propagation by callosal optogenetic stimulation and related synaptic spread

208   of activity presents a caveat for the conclusion of circuit specificity for *in vivo* optogenetic studies. In particular,

209   when neuronal projection terminals labeled with ChR-2 from neurons located at specific functional nuclei are

210   targeted, possible spreading network activity from the antidromically activated brain sites need to be considered. In

211   our experiments, BOLD signals were detected in both MC and PO projected from the antidromically activated BC

212   (at 5Hz light pulses), indicating a (for the experimental purpose unintended) wide-spread optogenetic activation

213   pattern in the brain-wide network (**Fig 1e**). This spread is likely due to synaptic propagation via activated local or

214   regional axon collaterals of CPNs [71-75]. For the present spread into motor and sensorimotor structures, deep layer

215   CPN with long-range projections into sensorimotor brain areas are likely involved [76]. In addition, multi-synaptic

216   pathways, involving either cortico-cortical or cortico-thalamic projections may have contributed to the spread brain-

217   wide activation [77, 78]. In conclusion, it is mandatory to consider brain-wide activation patterns, even in case of

218   application of highly circuit-specific optogenetic activation schemes.

219   Certainly, the optogenetic callosal fiber activation also elicits the specific unidirectional callosal orthodromic

220   activity as well, similar to earlier reports[43, 44, 46]. In addition, the optogenetic activation of the callosal projection

221   terminals from brain slices leads to better characterization of the excitatory and inhibitory circuit regulation by

222   callosal inputs [56, 58-60, 79]. Our observations further support the non-linear neurovascular coupling events with

223   the optical intrinsic signal measurements and laser-doppler flowmetry upon the optogenetic or electrical CC

224   stimulation [43, 55]. In our study, the fact that orthodromic BOLD signals were readily observed with low-

225   frequency stimulation (2 Hz), but were strongly reduced at the higher frequency (5Hz), reveals a critical non-linear

226   manner of the hemodynamic responses driven the the CC-mediated neuronal activation(**Fig. 1f**, **2c**, and **Fig. S6**).

227   We show here that peripheral whisker stimulation is well suited to study the suppressive effects of orthodromically

228   conveyed activity specific to the callous, which is not possible using *in vivo* bilateral stimulation paradigms in

229   rodents [50-54] or bilateral motor or visual tasks in humans [47-49] where other pathways maybe involved. In

230   particular, CC-induced orthodromic activity of L5 pyramidal neurons evoked a calcium transient followed by

231   marked depression of calcium signals responding to light pulses on CC (**Fig. 2c,d**) (consistent with the optogenetic

232   results in brain slices [59]). Electrophysiology in brain slices has elucidated that CC-mediated glutamatergic

233   excitatory postsynaptic potentials are followed by early $GABA_A$- and late $GABA_B$-mediated inhibitory postsynaptic

234   potentials lasting for several hundred milliseconds [44-46, 60], strongly suggesting that the depression seen here is

235   partly due to synaptic inhibition. Also, while pairing with 2 Hz whisker stimulation, a time course of the depressive

236   effect around 50-100 ms interval fit the previous finding that local intracortical activation is characterized by

237   activation of long-lasting synaptic GABAergic inhibition [57, 68, 69, 80-82]. In particular, besides the robust

238   inhibition detected in the paired O50W and O100W conditions, a refined temporal scale at the O25W condition

239   further demonstrates the CC-mediated inhibitory effect (**Fig. S12**), which can be potentially caused by the $GABA_A$-

240   mediated early IPSP peak elicited by the direct electrical CC stimulation [44]. The fact that antidromic activity is

241   not susceptible for the paired optogenetic and whisker stimulation (surely due to weaker ipsilateral whisker-evoked

242   activity, but also likely due to the relative strength of antidromic activation), supports the notion that the depression

243 of whisker-evoked activity is due mainly to local (contralateral) interaction of CC-evoked and whisker-evoked
244 activity, rather than to possible CC activity evoked by indirect activation of additional CPNs via antidromic
245 activation.

246 The whole-brain fMRI with concurrent calcium recording allows accessing brain-wide network effects of CC-
247 mediated inhibition (**Fig. 4a, b**). In particular, the applicaton of the AM-based GLM allows separating the stimulus-
248 driven reponses from the AM factor, which creates specific correlation maps to the CC-mediated inhibitory effects.
249 The calcium amplitude-modulation (AM)-based correlation map highlighted three brain regions: the ventral part of
250 right BC, the left MC, and PO. The ventral right BC was likely activated by reciprocal callosal connections, the
251 majority of which, as argued above, may have been quenched by the strong antidromic effect via labeled CPNs. In
252 the injection experiments, however, the ventral BC was regularly spared and did not receive virus, and therefore
253 may have been less affected by overriding antidromic activity. Outside BC on the orthodromic side the AM-
254 dependent correlation was detected as well in the right MC and PO. The CC-mediated inhibitory effect on the
255 spatially distinct MC could be caused by the long-range S1-MC projection for sensorimotor integration [78, 83-86].
256 The direct BOLD activation in the MC was detected by whisker stimulation through the sensorimotor connection
257 [87], which was also shown in the antidromic activity-based spreading activation patterns (**Fig 1e**). The CC-
258 mediated inhibitory effect on the PO is likely via corticothalamic projections originating from BC layer 5b neurons
259 [88-91]. This finding points at a potential participation of the callosal inputs in the regulation of a wider network of
260 a reciprocal thalamocortical network which mediates BC signals from the other hemisphere for whisking related
261 processing [77, 83, 89, 92-95]. Therefore, besides the antidromically evoked network activation pattern, the
262 orthodromic CC-mediated inhibition generates a brain-wide activity pattern of its own.

263 In summary, by taking advantage of optogenetics to activate unidirectional callosal fiber, calcium indicators
264 (GCaMP6f) to track specific L5 pyramidal neuronal activity, and simultaneous whole-brain fMRI mapping, this
265 work bridges the scales from the cellular to the whole brain network level for CC-mediated activity. We present a
266 multi-modal fMRI platform to map and analyze the CC-regulated excitation/inhibition balance across multiple
267 scales, which should be useful to decipher brain network dysfunction induced from CC abnormalities. Brain-wide
268 network activation from callosal-circuit optogenetic stimulation underscores the caution to interpret circuit-specific
269 regulatory mechanisms underlying behavioral or functional outcomes with optogenetics in animals.

270 **Materials and methods**

271 **Animal procedures.** The study was performed in accordance with the German Animal Welfare Act (TierSchG)
272 and Animal Welfare Laboratory Animal Ordinance (TierSchVersV). This is in full compliance with the guidelines
273 of the EU Directive on the protection of animals used for scientific purposes (2010/63/EU). The study was reviewed
274 by the ethics commission (§15 TierSchG) and approved by the state authority (Regierungspräsidium, Tübingen,

275 Baden-Württemberg, Germany). A 12-12 hour on/off lighting cycle was maintained to assure undisturbed circadian
276 rhythm. The food and water were obtainable ad libitum. A total of 24 (17 for fMRI and 7 for electrophysiology)
277 male Sprague–Dawley rats were used in this study.

278 **Viral injection.** Intracerebral viral injection was performed in 4-week-old rats to express the viral vectors
279 containing the light-sensitive protein channelrhodopsin-2 (ChR2, for optogenetics) and/or the calcium-sensitive
280 protein (GCaMP, for calcium recording) in neurons. The construct AAV5.Syn.GCaMP6f.WPRE.SV40 was used to
281 express GCaMP in the left BC and the constructs AAV5.CaMKII.hChR2(H134R)-mCherry.WPRE.hGH was used
282 to express ChR2 in the right BC. The stereotaxic coordinates of the injections were ±2.5 mm posterior to Bregma,
283 5.0 mm lateral to the midline, 0.8-1.4 mm below the cortical surface. Rats were anesthetized with 1.5-2% isoflurane
284 via nose cone and placed on a stereotaxic frame, an incision was made on the scalp and the skull was exposed.
285 Craniotomies were performed with a pneumatic drill so as to cause minimal damage to cortical tissue. A volume of
286 0.6-0.9 µL and 0.6 µL, for optogenetics and calcium signal recording, respectively, was injected using a 10 µL
287 syringe and 33-gauge needle. The injection rate was controlled by an infusion pump (Pump 11 Elite, Harvard
288 Apparatus, USA). After injection, the needle was left in place for approximately 5 min before being slowly
289 withdrawn. The craniotomies were sealed with bone wax and the skin around the wound was sutured. Rats were
290 subcutaneously injected with antibiotic and painkiller for 3 consecutive days to prevent bacterial infections and
291 relieve postoperative pain.

292 **Immunohistochemistry.** To verify the phenotype of the transfected cells, opsin localization and optical fiber
293 placement, perfused rat brains were fixed overnight in 4% paraformaldehyde and then equilibrated in 15% and 30%
294 sucrose in 0.1 M PBS at 4ºC. 30 µm-thick coronal sections were cut on a cryotome (CM3050S, Leica, Germany).
295 Free-floating sections were washed in PBS, mounted on microscope slides, and incubated with DAPI (VectaShield,
296 Vector Laboratories, USA) for 30 mins at room temperature. Wide-field fluorescent images were acquired using a
297 microscope (Zeiss, Germany) for assessment of GCaMP and ChR2 expression in BC. Digital images were
298 minimally processed using ImageJ to enhance brightness and contrast for visualization purposes.

299 **Optical setup for calcium recordings.** A laser was used as excitation light source (OBIS 488LS, Coherent,
300 Germany) with a heat sink to enable laser operation throughout the entire specified temperature range from 10°C
301 to 40°C. The light passed through a continuously variable neutral density filter (NDC-50C-2M-B, Thorlabs,
302 Germany) and was reflected on a dichroic beam splitter (F48-487, AHF analysentechnik AG, Germany). The beam
303 was collected into an AR coated achromatic lens (AC254-030-A, Thorlabs, Germany) fixed on a threaded flexure
304 stage (HCS013, Thorlabs, Germany) mounted on an extension platform (AMA009/M, Thorlabs, Germany) of a
305 fiber launch system (MAX350D/M, Thorlabs, Germany). The laser beam was projected into the fiber and
306 propagated to its tip. The fluorescence emitted by neurons was collected through the fiber tip, propagated back and

307 collimated by the achromatic lens, passed through the dichroic beam splitter and filtered by a band-pass filter

308 (ET525/50M, Chroma, USA) and focused by an AR coated achromatic lens (AC254-030-A, Thorlabs, Germany).

309 A silicon photomultiplier module (MiniSM 10035, SensL, Germany) was applied to detect the emitted fluorescence.

310 The entire optical system was enclosed in a light isolator box. The photomultiplier output was amplified (gain =

311 100) by a voltage amplifier (DLPVA-100-BLN-S, Femto, Germany), digitized and detected by BIOPAC system

312 (MP150 System, BIOPAC Systems, USA).

313 **Animal preparation and fiber optic implantation for fMRI.** Anesthesia was first induced in the animal with 5%

314 isoflurane in the chamber. The anesthetized rat was intubated using a tracheal tube and a mechanical ventilator

315 (SAR-830, CWE, USA) was used to ventilate animals throughout the whole experiment. Femoral arterial and

316 venous catheterization was performed with polyethylene tubing for blood sampling, drug administration, and

317 constant blood pressure measurements. After the surgery, isoflurane was switched off, and a bolus of the anesthetic

318 alpha-chloralose (80 mg/kg) was infused intravenously. A mixture of alpha-chloralose (26.5 mg/kg/h) and

319 pancuronium (2 mg/kg/h) was constantly infused to maintain the anesthesia/keep the animal anesthetized and reduce

320 motion artifacts.

321 Before transferring the animal to the MRI scanner, two craniotomies were performed: one for fixed fiber

322 implantation to record calcium signals from BC, and the other one for dynamic insertion of the optical fiber to

323 stimulate the CC using optogenetics (dynamic insertion was achieved by using a remote positioning tool [62]). The

324 animal was placed on a stereotaxic frame, the scalp was opened and two ~1.5 mm diameter burr holes were drilled

325 on the skull. The dura was carefully removed and an optical fiber with 200 µm core diameter (FT200EMT, Thorlabs,

326 Germany) was inserted into the BC, at coordinates: 2.75-3.3 mm posterior to Bregma, 5.0 mm lateral to the midline,

327 1.2-1.4 mm below the cortical surface. An adhesive gel was used to secure the calcium recording fiber to the skull.

328 The craniotomy for optogenetics on CC in the other hemisphere, at coordinates: 2.75-3.3 mm posterior to Bregma,

329 1.8-2.4 mm lateral to the midline, was covered by agarose gel for the robotic arm-driven fiber insertion inside the

330 MRI scanner. The eyes of the rats were covered to prevent stimulation of the visual system during the optogenetic

331 fMRI, which can occur in cases with imperfect coverage or under the strong power of light pulses through tissue.

332 **Functional MRI acquisition**. All images were acquired with a 14.1 T/26 cm horizontal bore magnet interfaced to

333 an Avance III console and equipped with a 12 cm gradient set capable of providing 100 G/cm over a time of 150

334 µs. A transceiver single-loop surface coil with an inner diameter of 22 mm was placed directly over the rat head to

335 acquire anatomical and fMRI images. Magnetic field homogeneity was optimized first by global shimming for

336 anatomical images and followed by FASTMAP shimming protocol for the EPI sequence. Functional images were

337 acquired with a 3D gradient-echo EPI sequence with the following parameters: Echo Time 11.5 ms, repetition time

338 1.5 s, FOV 1.92 cm $\times$ 1.92 cm $\times$ 1.92 cm, matrix size $48 \times 48 \times 48$, spatial resolution 0.4 mm $\times$ 0.4 mm $\times$ 0.4 mm.

11

339   For anatomical reference, the RARE sequence was applied to acquire 48 coronal slices with the same geometry as

340   that of the fMRI images. The paradigm for each trial consisted of 360 dummy scans to reach steady-state, 10 pre-

341   stimulation scans, 5 scans during stimulation (stimulation period 8 s), 35 post-stimulation scans with total 13 epochs

342   and 15 epochs for refined stimulus design (See **Stimulation protocols**).

343   For fMRI and electrophysiology studies, needle electrodes were placed on whisker pads of the rats, and electric

344   pulses (333 µs duration at 1.5 mA repeated at 3 Hz for 4 seconds) were first used as stimulation to serve as a positive

345   control for the evoked BOLD signal or local field potential/calcium signal. Once that reliable fMRI signals and

346   calcium signals were observed in response to electrical stimulation, optical stimulation was performed. For

347   optogenetic stimulation, square pulses of blue light (473 nm) were delivered using a laser (MBL-III, CNI, China)

348   connected to the 200 µm core optical fiber (FT200EMT, Thorlabs, Germany) and controlled by Master 9 (Master-

349   9, A.M.P.I., Israel) to deliver blue light pulses at 1-40 Hz, 1-20 ms pulse width with 2-8 s duration. The light

350   intensity was tested before each experiment and was calibrated with a power meter (PM20A, Thorlabs, Germany)

351   to emit 0.6 mW to 40 mW from the tip of the optical fiber for CC activation.

352   **Stimulation protocols.** A 2 Hz, 8 s optogenetic stimulus train (O train; 16 pulses to the corpus callosum) was

353   delivered preceding a conditioning stimulus train (W train; same pulse parameters were used, 0.75-1.5 mA) while

354   varying the time interval between stimuli (0, 10, 25, 50, 100 and 200 ms), or without a W train, in a single trial.

355   These stimulation conditions were automatically executed using a laser (MBL-III, CNI, China) and a stimulator

356   (A365 Stimulus Isolator, WPI, USA) triggered by a combination program provided by pulse generator (Master-9,

357   A.M.P.I., Israel), which were precisely synchronized with the start time of the image acquisition sequence in each

358   trial. Each trial consisted of the first fixed whisker stimuli block (W) and 12 blocks randomized for 6 different

359   conditions, W, O, WO, W50O, W100O, W200O, in total 13 min and 15 s for each trial. For refined inter-stimulus

360   intervals design, first fixed whisker stimuli block (W) and 14 blocks randomized for 7 different conditions were

361   used: W, OW, O10W, O25W, O50W, O100W, and O200W, in total 15 min 15 s for each trial. The tables below

362   show the number of continuous trials acquired in this study, as well as light power for optogenetic stimulation.

363   Table 1. The number of trials acquired for 6 conditions.

	Rat#1	Rat #2	Rat #3	Rat #4	Rat #5	Rat #6
Trials	6	4	4	4	6	5
Acquiring Time	79m 30s	53m	53m	53m	79m 30s	66m 15s

364

365   Table 2. The number of trials acquired with refined stimulus design.

	Rat#7	Rat #8	Rat #9	Rat #10 (LFP)

12

Trials	9	12	5	7
Acquiring Time	137m 15s	183m	76m 15s	106m 45s

366

367 Table 3. Light power for optogenetic stimulation.

	L6	L6.5	L7	L7.5	L8	L8.5	L9	L9.5	L9.9	L10
Light power (mW)	2.6	5.4	9.2	13.2	17.6	23.7	29.2	35.3	39.9	>40

368

369 **Simultaneous calcium recording with electrophysiology.** The anesthetic and surgical preparation procedures
370 were similar to the fMRI experiments. For antidromic activity recording experiments in **Fig. 1** and **Fig. S2-5**,
371 tungsten microelectrode (UEWSDDSMCN1M, FHC, USA) was implanted in the right BC to record the LFP from
372 the callosal projection neurons. For orthodromic activity in **Fig.2** and **Fig. S7-10**, the same kind of tungsten
373 microelectrode was attached to the fiber optic closely, implanted in the left BC, then secured to the skull by an
374 adhesive gel. To calculate the coordinates of optical fiber implantation for CC activation, a FLASH anatomical MRI
375 image was acquired to confirm the virus injection one day before the experiment. The LFP was recorded and
376 amplified through the EEG module of the BIOPAC system (gain factor, 5000, band-pass filter, 0.02-100 Hz,
377 sampling rate, 5,000/s). In parallel, the GCaMP6f-mediated fluorescent signal and blood pressure were digitized
378 and recorded with BIOPAC (MP150 System, BIOPAC Systems, USA) at a sampling rate of 5 kHz. The experiment
379 design and equipment used afterward were similar to the fMRI experiments.

380 **Data analysis.** Acquired data were analyzed using Functional NeuroImages software (AFNI, NIH, USA) and
381 custom-written Matlab (MATLAB, MathWorks, USA) programs for calcium signals. The fiber optical neuronal
382 calcium signals were low-pass filtered at 100 Hz using zero-phase shift digital filtering (filtfilt function in
383 MATLAB). The relative percentage change of fluorescence ($\Delta F/F$) was defined as $(F-F_0)/F_0$, where F_0 is the baseline,
384 i.e., the average fluorescent signal in a 2 s pre-stimulation window. For **Fig. 2d**, the spike value is defined by the
385 maximal value for the difference in $\Delta F/F$ in a time window 0.3 s after the stimulus, as shown from 40 Hz in **Fig.**
386 **2c**, while the baseline drift is the average calcium signal from 0.3–8 s after the spike recovered to baseline for 40
387 Hz stimulation. For **Fig. 3e**, the first epoch for each trial (fixed W condition) was excluded in the data analysis and
388 the calcium signal was averaged for each condition from all the acquired trials for each animal. Each condition was
389 then normalized by the maximum positive deflection of calcium signal alone conditions. For **Fig. 3f, h, i**, the
390 amplitude peak of the neuronal fluorescent signal in response to 8 s whisker stimulus was calculated as the maximal
391 difference in $\Delta F/F$ in a time window 300 ms after stimulus, then normalized to the whisker only (W) condition
392 (100%). The unnormalized amplitude for the difference in $\Delta F/F$ for each epoch was used to generate the calcium
393 signal-based regressor (**Fig. S14**) for fMRI correlation map in **Fig. 4**.

13

394   For evoked fMRI analysis, EPI images were first aligned to anatomical images acquired in the same orientation

395   with the same geometry. The anatomical MRI images were registered to a template across animals, as well as EPI

396   datasets. The baseline signal of EPI images was normalized to 100 for statistical analysis of the multiple trials of

397   EPI time courses. The time courses of the BOLD signal were extracted from regions of interest, e.g., barrel cortex,

398   motor cortex, and posterior thalamus, which were segmented on the anatomical images based on the brain atlas and

399   activation or correlation values. The BOLD amplitude for each condition was defined as the average value for the

400   volumes within the 0-10.5 s following the onset of stimulation (when stimulation duration was 8 s). The

401   hemodynamic response function (HRF) used was the default of the block function of the linear program

402   3dDeconvolve in AFNI. BLOCK (L, 1) computes a convolution of a square wave of duration L and makes a peak

403   amplitude of block response $= 1$, with $g(t) = t^4 e^{-t} / [4^4 e^{-4}]$ (peak value=1). In this case, each beta weight

404   represents the peak height of the corresponding BLOCK curve for that class, i.e. the beta weight is the magnitude

405   of the response to the entire stimulus block, as shown in **Fig. 1, 3** and **Fig. S1**. The HRF model is defined as follows:

406
$$HRF(t) = int(g(t - s), s = 0 .. \min(t, L))$$

407   For correlation analysis, a calcium signal amplitude modulated regressor (AM2) based AFNI BLOCK (L, 1)

408   function was used (**Fig. S14**). The regressor for amplitude modulated response model is as follows:

409
$$r_{AM2}(t) = \sum_{k=1}^{K} h(t - \tau_k) \cdot (a_k - \bar{a})$$

410   Where $a_k = $ value of kth auxiliary behavioral information value (ABI), i.e., calcium amplitude value for the

411   difference in $\Delta F/F$ for each epoch, and $\bar{a}$ is the average calcium amplitude value for all the epochs for the individual

412   animal. The statistics and β for AM2 regressor make activation map of voxels whole BOLD response vary

413   proportionally to ABI, i.e., the changes in calcium signals for each epoch.

414   **Author Contributions**

415   X.Y. designed and supervised the research, Y.C. and X.Y. performed animal experiments, Y.C. acquired data, Y.C.

416   analyzed data, A.K., C.S., F.S. and P.P-R. provided conceptual and technical support, X.Y., Y.C., A.K. and C.S.

417   wrote the manuscript.

418   **Data availability.** Excel files are included for each quantitative plot included in the main figures. All other data

419   generated during this study are available from the corresponding author upon reasonable request.

420   **Code availability.** The Analysis of Functional NeuroImages software (AFNI, NIH, USA) and Matlab (MATLAB,

421   MathWorks, USA) were used to process the fMRI and simultaneously acquired calcium signals, respectively. The

422 relevant source codes can be downloaded through https://afni.nimh.nih.gov/afni/. The related image processing
423 codes are available from the corresponding author upon reasonable request.

424 **Competing interests.** The authors declare no competing interests.

425 **ACKNOWLEDGEMENTS**

432 **REFERENCES**

433 1. Nagel, G., et al., *Channelrhodopsin-1: a light-gated proton channel in green algae.* Science, 2002.
434   **296**(5577): p. 2395-8.
435 2. Boyden, E.S., et al., *Millisecond-timescale, genetically targeted optical control of neural activity.* Nat
436   Neurosci, 2005. **8**(9): p. 1263-8.
437 3. Zhang, F., et al., *Channelrhodopsin-2 and optical control of excitable cells.* Nat Methods, 2006. **3**(10): p.
438   785-92.
439 4. Li, X., et al., *Fast noninvasive activation and inhibition of neural and network activity by vertebrate
440   rhodopsin and green algae channelrhodopsin.* Proc Natl Acad Sci U S A, 2005. **102**(49): p. 17816-21.
441 5. Adamantidis, A.R., et al., *Neural substrates of awakening probed with optogenetic control of hypocretin
442   neurons.* Nature, 2007. **450**(7168): p. 420-4.
443 6. Lima, S.Q. and G. Miesenbock, *Remote control of behavior through genetically targeted photostimulation
444   of neurons.* Cell, 2005. **121**(1): p. 141-52.
445 7. Nagel, G., et al., *Light activation of channelrhodopsin-2 in excitable cells of Caenorhabditis elegans triggers
446   rapid behavioral responses.* Curr Biol, 2005. **15**(24): p. 2279-84.
447 8. Tsai, H.C., et al., *Phasic firing in dopaminergic neurons is sufficient for behavioral conditioning.* Science,
448   2009. **324**(5930): p. 1080-4.
449 9. Carter, M.E., et al., *Tuning arousal with optogenetic modulation of locus coeruleus neurons.* Nat Neurosci,
450   2010. **13**(12): p. 1526-33.
451 10. Tye, K.M. and K. Deisseroth, *Optogenetic investigation of neural circuits underlying brain disease in animal
452   models.* Nat Rev Neurosci, 2012. **13**(4): p. 251-66.
453 11. Kim, C.K., A. Adhikari, and K. Deisseroth, *Integration of optogenetics with complementary methodologies
454   in systems neuroscience.* Nat Rev Neurosci, 2017. **18**(4): p. 222-235.
455 12. Cardin, J.A., et al., *Targeted optogenetic stimulation and recording of neurons in vivo using cell-type-
456   specific expression of Channelrhodopsin-2.* Nat Protoc, 2010. **5**(2): p. 247-54.
457 13. Bernal-Casas, D., et al., *Studying Brain Circuit Function with Dynamic Causal Modeling for Optogenetic
458   fMRI.* Neuron, 2017. **93**(3): p. 522-532 e5.
459 14. Inoue, K.I., M. Takada, and M. Matsumoto, *Neuronal and behavioural modulations by pathway-selective
460   optogenetic stimulation of the primate oculomotor system.* Nat Commun, 2015. **6**: p. 8378.

461 15. Sych, Y., et al., *High-density multi-fiber photometry for studying large-scale brain circuit dynamics.* Nat
462   Methods, 2019. **16**(6): p. 553-560.
463 16. Gao, R., et al., *Cortical column and whole-brain imaging with molecular contrast and nanoscale resolution.*
464   Science, 2019. **363**(6424).
465 17. Yu, X., et al., *Sensory and optogenetically driven single-vessel fMRI.* Nat Methods, 2016. **13**(4): p. 337-40.
466 18. Lee, J.H., et al., *Global and local fMRI signals driven by neurons defined optogenetically by type and wiring.*
467   Nature, 2010. **465**(7299): p. 788-92.
468 19. Albers, F., et al., *Line scanning fMRI reveals earlier onset of optogenetically evoked BOLD response in rat
469   somatosensory cortex as compared to sensory stimulation.* Neuroimage, 2018. **164**: p. 144-154.
470 20. Ryali, S., et al., *Combining optogenetic stimulation and fMRI to validate a multivariate dynamical systems
471   model for estimating causal brain interactions.* Neuroimage, 2016. **132**: p. 398-405.
472 21. Grandjean, J., et al., *A brain-wide functional map of the serotonergic responses to acute stress and
473   fluoxetine.* Nat Commun, 2019. **10**(1): p. 350.
474 22. Just, N. and C. Faber, *Probing activation-induced neurochemical changes using optogenetics combined
475   with functional magnetic resonance spectroscopy: a feasibility study in the rat primary somatosensory
476   cortex.* J Neurochem, 2019. **150**(4): p. 402-419.
477 23. Schulz, K., et al., *Simultaneous BOLD fMRI and fiber-optic calcium recording in rat neocortex.* Nat Methods,
478   2012. **9**(6): p. 597-602.
479 24. Wang, M., et al., *Brain-state dependent astrocytic Ca(2+) signals are coupled to both positive and negative
480   BOLD-fMRI signals.* Proc Natl Acad Sci U S A, 2018. **115**(7): p. E1647-E1656.
481 25. He, Y., et al., *Ultra-Slow Single-Vessel BOLD and CBV-Based fMRI Spatiotemporal Dynamics and Their
482   Correlation with Neuronal Intracellular Calcium Signals.* Neuron, 2018. **97**(4): p. 925-939 e5.
483 26. Schwalm, M., et al., *Cortex-wide BOLD fMRI activity reflects locally-recorded slow oscillation-associated
484   calcium waves.* Elife, 2017. **6**.
485 27. Albers, F., et al., *Multimodal Functional Neuroimaging by Simultaneous BOLD fMRI and Fiber-Optic
486   Calcium Recordings and Optogenetic Control.* Mol Imaging Biol, 2018. **20**(2): p. 171-182.
487 28. van Alst, T.M., et al., *Anesthesia differentially modulates neuronal and vascular contributions to the BOLD
488   signal.* Neuroimage, 2019. **195**: p. 89-103.
489 29. Schmid, F., et al., *Assessing sensory versus optogenetic network activation by combining (o)fMRI with
490   optical Ca2+ recordings.* J Cereb Blood Flow Metab, 2016. **36**(11): p. 1885-1900.
491 30. Sperry, R.W., *Cerebral Organization and Behavior: The split brain behaves in many respects like two
492   separate brains, providing new research possibilities.* Science, 1961. **133**(3466): p. 1749-57.
493 31. Gazzaniga, M.S., *Forty-five years of split-brain research and still going strong.* Nat Rev Neurosci, 2005. **6**(8):
494   p. 653-9.
495 32. Karolis, V.R., M. Corbetta, and M. Thiebaut de Schotten, *The architecture of functional lateralisation and
496   its relationship to callosal connectivity in the human brain.* Nat Commun, 2019. **10**(1): p. 1417.
497 33. Innocenti, G.M., F. Ansermet, and J. Parnas, *Schizophrenia, neurodevelopment and corpus callosum.* Mol
498   Psychiatry, 2003. **8**(3): p. 261-74.
499 34. Pomarol-Clotet, E., et al., *Medial prefrontal cortex pathology in schizophrenia as revealed by convergent
500   findings from multimodal imaging.* Mol Psychiatry, 2010. **15**(8): p. 823-30.
501 35. Egaas, B., E. Courchesne, and O. Saitoh, *Reduced size of corpus callosum in autism.* Arch Neurol, 1995.
502   **52**(8): p. 794-801.
503 36. Anderson, J.S., et al., *Decreased interhemispheric functional connectivity in autism.* Cereb Cortex, 2011.
504   **21**(5): p. 1134-46.
505 37. Spencer, S.S., et al., *Corpus Callosotomy for Epilepsy .1. Seizure Effects.* Neurology, 1988. **38**(1): p. 19-24.
506 38. van Eijsden, P., et al., *In vivo diffusion tensor imaging and ex vivo histologic characterization of white
507   matter pathology in a post-status epilepticus model of temporal lobe epilepsy.* Epilepsia, 2011. **52**(4): p.
508   841-5.

509   39.   Schaefer, G.B. and J.B. Bodensteiner, *Developmental anomalies of the brain in mental retardation.*
510   International Review of Psychiatry, 1999. **11**(1): p. 47-55.
511   40.   van Schooneveld, M.M., et al., *Hemispherectomy: a basis for mental development in children with epilepsy.*
512   Epileptic Disord, 2011. **13**(1): p. 47-55.
513   41.   Gazzaniga, M.S., *Cerebral specialization and interhemispheric communication: does the corpus callosum*
514   *enable the human condition?* Brain, 2000. **123 (Pt 7)**: p. 1293-326.
515   42.   Schulte, T., E.M. Muller, and E.M. Oehring, *Contribution of callosal connections to the interhemispheric*
516   *integration of visuomotor and cognitive processes.* Neuropsychol Rev, 2010. **20**(2): p. 174-90.
517   43.   Hoffmeyer, H.W., et al., *Nonlinear neurovascular coupling in rat sensory cortex by activation of*
518   *transcallosal fibers.* J Cereb Blood Flow Metab, 2007. **27**(3): p. 575-87.
519   44.   Kawaguchi, Y., *Receptor subtypes involved in callosally-induced postsynaptic potentials in rat frontal*
520   *agranular cortex in vitro.* Exp Brain Res, 1992. **88**(1): p. 33-40.
521   45.   Kumar, S.S. and J.R. Huguenard, *Properties of excitatory synaptic connections mediated by the corpus*
522   *callosum in the developing rat neocortex.* J Neurophysiol, 2001. **86**(6): p. 2973-85.
523   46.   Karayannis, T., I. Huerta-Ocampo, and M. Capogna, *GABAergic and pyramidal neurons of deep cortical*
524   *layers directly receive and differently integrate callosal input.* Cereb Cortex, 2007. **17**(5): p. 1213-26.
525   47.   Ni, Z., et al., *Two phases of interhemispheric inhibition between motor related cortical areas and the*
526   *primary motor cortex in human.* Cereb Cortex, 2009. **19**(7): p. 1654-65.
527   48.   Schnitzler, A., K.R. Kessler, and R. Benecke, *Transcallosally mediated inhibition of interneurons within*
528   *human primary motor cortex.* Exp Brain Res, 1996. **112**(3): p. 381-91.
529   49.   Bocci, T., et al., *Transcallosal inhibition dampens neural responses to high contrast stimuli in human visual*
530   *cortex.* Neuroscience, 2011. **187**: p. 43-51.
531   50.   Ogawa, S., et al., *An approach to probe some neural systems interaction by functional MRI at neural time*
532   *scale down to milliseconds.* Proc Natl Acad Sci U S A, 2000. **97**(20): p. 11026-31.
533   51.   Shuler, M.G., D.J. Krupa, and M.A. Nicolelis, *Bilateral integration of whisker information in the primary*
534   *somatosensory cortex of rats.* J Neurosci, 2001. **21**(14): p. 5251-61.
535   52.   Wiest, M.C., N. Bentley, and M.A. Nicolelis, *Heterogeneous integration of bilateral whisker signals by*
536   *neurons in primary somatosensory cortex of awake rats.* J Neurophysiol, 2005. **93**(5): p. 2966-73.
537   53.   Berwick, J., et al., *Integration of neural responses originating from different regions of the cortical*
538   *somatosensory map.* Brain Res, 2004. **1030**(2): p. 284-93.
539   54.   Nemoto, M., et al., *Diversity of neural-hemodynamic relationships associated with differences in cortical*
540   *processing during bilateral somatosensory activation in rats.* Neuroimage, 2012. **59**(4): p. 3325-38.
541   55.   Iordanova, B., et al., *Optogenetic investigation of the variable neurovascular coupling along the*
542   *interhemispheric circuits.* J Cereb Blood Flow Metab, 2018. **38**(4): p. 627-640.
543   56.   Petreanu, L., et al., *Channelrhodopsin-2-assisted circuit mapping of long-range callosal projections.* Nat
544   Neurosci, 2007. **10**(5): p. 663-8.
545   57.   Palmer, L.M., J.M. Schulz, and M.E. Larkum, *Layer-specific regulation of cortical neurons by*
546   *interhemispheric inhibition.* Commun Integr Biol, 2013. **6**(3): p. e23545.
547   58.   Rock, C. and A.J. Apicella, *Callosal projections drive neuronal-specific responses in the mouse auditory*
548   *cortex.* J Neurosci, 2015. **35**(17): p. 6703-13.
549   59.   Lee, A.T., et al., *Pyramidal neurons in prefrontal cortex receive subtype-specific forms of excitation and*
550   *inhibition.* Neuron, 2014. **81**(1): p. 61-8.
551   60.   Palmer, L.M., et al., *The cellular basis of GABA(B)-mediated interhemispheric inhibition.* Science, 2012.
552   **335**(6071): p. 989-93.
553   61.   Xin Yu, S.D., and Alan P. Koretsky, *Targeting Projection Fibers for Optogenetics and fMRI.* Proc. Intl. Soc.
554   Mag. Reson. Med. 21, 2013.
555   62.   Chen, Y., et al., *MRI-guided robotic arm drives optogenetic fMRI with concurrent Ca2+ recording.* Nature
556   Communications, 2019. **10**.

17

557 63. Yu, X., et al., *Thalamocortical inputs show post-critical-period plasticity.* Neuron, 2012. **74**(4): p. 731-42.

558 64. Simmons, P.A. and A.L. Pearlman, *Receptive-field properties of transcallosal visual cortical neurons in the*
559 *normal and reeler mouse.* J Neurophysiol, 1983. **50**(4): p. 838-48.

560 65. Caminiti, R., et al., *Diameter, length, speed, and conduction delay of callosal axons in macaque monkeys*
561 *and humans: comparing data from histology and magnetic resonance imaging diffusion tractography.* J
562 Neurosci, 2013. **33**(36): p. 14501-11.

563 66. Suarez, R., et al., *Balanced interhemispheric cortical activity is required for correct targeting of the corpus*
564 *callosum.* Neuron, 2014. **82**(6): p. 1289-98.

565 67. Fox, K., *Barrel Cortex.* Barrel Cortex, 2008: p. 1-+.

566 68. Butovas, S. and C. Schwarz, *Spatiotemporal effects of microstimulation in rat neocortex: a parametric*
567 *study using multielectrode recordings.* J Neurophysiol, 2003. **90**(5): p. 3024-39.

568 69. Butovas, S., et al., *Effects of electrically coupled inhibitory networks on local neuronal responses to*
569 *intracortical microstimulation.* J Neurophysiol, 2006. **96**(3): p. 1227-36.

570 70. Cox, R.W., *AFNI: software for analysis and visualization of functional magnetic resonance neuroimages.*
571 Comput Biomed Res, 1996. **29**(3): p. 162-73.

572 71. Mitchell, B.D. and J.D. Macklis, *Large-scale maintenance of dual projections by callosal and frontal cortical*
573 *projection neurons in adult mice.* Journal of Comparative Neurology, 2005. **482**(1): p. 17-32.

574 72. Cauller, L.J., B. Clancy, and B.W. Connors, *Backward cortical projections to primary somatosensory cortex*
575 *in rats extend long horizontal axons in layer I.* Journal of Comparative Neurology, 1998. **390**(2): p. 297-310.

576 73. Fame, R.M., J.L. MacDonald, and J.D. Macklis, *Development, specification, and diversity of callosal*
577 *projection neurons.* Trends Neurosci, 2011. **34**(1): p. 41-50.

578 74. White, E.L. and D. Czeiger, *Synapses Made by Axons of Callosal Projection Neurons in Mouse*
579 *Somatosensory Cortex - Emphasis on Intrinsic Connections.* Journal of Comparative Neurology, 1991.
580 **303**(2): p. 233-244.

581 75. Wilson, C.J., *Morphology and Synaptic Connections of Crossed Corticostriatal Neurons in the Rat.* Journal
582 of Comparative Neurology, 1987. **263**(4): p. 567-580.

583 76. Veinante, P. and M. Deschenes, *Single-cell study of motor cortex projections to the barrel field in rats.*
584 Journal of Comparative Neurology, 2003. **464**(1): p. 98-103.

585 77. Gambino, F., et al., *Sensory-evoked LTP driven by dendritic plateau potentials in vivo.* Nature, 2014.
586 **515**(7525): p. 116-+.

587 78. Kleinfeld, D. and M. Deschenes, *Neuronal Basis for Object Location in the Vibrissa Scanning Sensorimotor*
588 *System.* Neuron, 2011. **72**(3): p. 455-468.

589 79. Petrus, E., et al., *Interhemispheric plasticity is mediated by maximal potentiation of callosal inputs.* Proc
590 Natl Acad Sci U S A, 2019. **116**(13): p. 6391-6396.

591 80. Logothetis, N.K., et al., *The effects of electrical microstimulation on cortical signal propagation.* Nat
592 Neurosci, 2010. **13**(10): p. 1283-91.

593 81. Cardin, J.A., et al., *Driving fast-spiking cells induces gamma rhythm and controls sensory responses.* Nature,
594 2009. **459**(7247): p. 663-7.

595 82. Moore, C.I., et al., *Neocortical interneurons: from diversity, strength.* Cell, 2010. **142**(2): p. 189-93.

596 83. Feldmeyer, D., et al., *Barrel cortex function.* Prog Neurobiol, 2013. **103**: p. 3-27.

597 84. Ferezou, I., et al., *Spatiotemporal dynamics of cortical sensorimotor integration in behaving mice.* Neuron,
598 2007. **56**(5): p. 907-23.

599 85. Chen, J.L., et al., *Behaviour-dependent recruitment of long-range projection neurons in somatosensory*
600 *cortex.* Nature, 2013. **499**(7458): p. 336-40.

601 86. Matyas, F., et al., *Motor control by sensory cortex.* Science, 2010. **330**(6008): p. 1240-3.

602 87. Yu, X., et al., *Deciphering laminar-specific neural inputs with line-scanning fMRI.* Nat Methods, 2014. **11**(1):
603 p. 55-8.

18

604   88.   Groh, A., et al., *Convergence of cortical and sensory driver inputs on single thalamocortical cells.* Cereb
605   Cortex, 2014. **24**(12): p. 3167-79.
606   89.   Sumser, A., et al., *Organization and somatotopy of corticothalamic projections from L5B in mouse barrel
607   cortex.* Proc Natl Acad Sci U S A, 2017. **114**(33): p. 8853-8858.
608   90.   Mease, R.A., et al., *Corticothalamic Spike Transfer via the L5B-POm Pathway in vivo.* Cereb Cortex, 2016.
609   **26**(8): p. 3461-75.
610   91.   Mease, R.A., et al., *Cortical Dependence of Whisker Responses in Posterior Medial Thalamus In Vivo.* Cereb
611   Cortex, 2016. **26**(8): p. 3534-43.
612   92.   Mease, R.A., M. Metz, and A. Groh, *Cortical Sensory Responses Are Enhanced by the Higher-Order
613   Thalamus.* Cell Rep, 2016. **14**(2): p. 208-15.
614   93.   Petreanu, L., et al., *The subcellular organization of neocortical excitatory connections.* Nature, 2009.
615   **457**(7233): p. 1142-5.
616   94.   Theyel, B.B., D.A. Llano, and S.M. Sherman, *The corticothalamocortical circuit drives higher-order cortex
617   in the mouse.* Nat Neurosci, 2010. **13**(1): p. 84-8.
618   95.   Manita, S., et al., *A Top-Down Cortical Circuit for Accurate Sensory Perception.* Neuron, 2015. **86**(5): p.
619   1304-16.

620

621   **Main Figures**
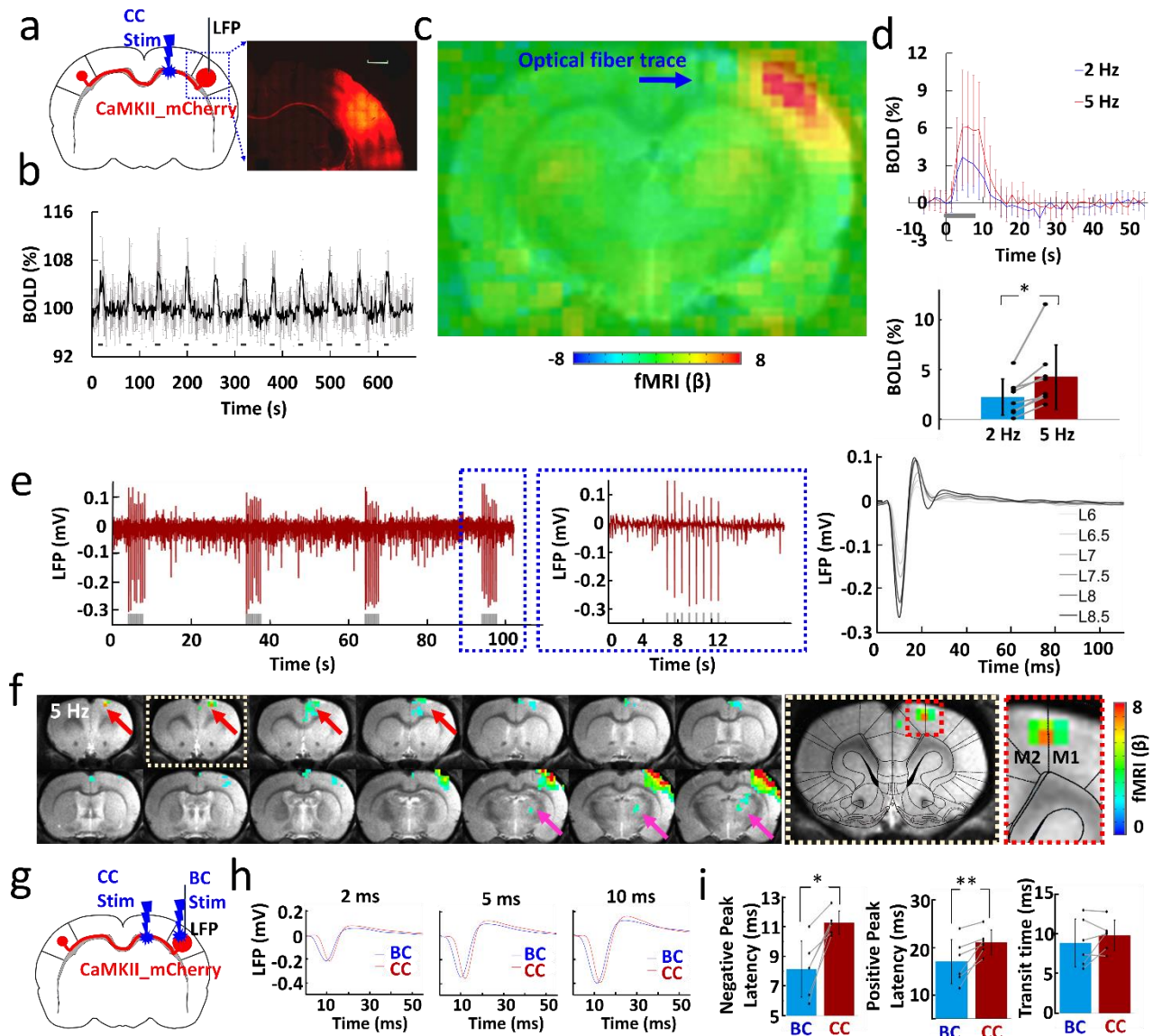
622

623   **Fig.1.** Antidromic activation upon corpus callosum optogenetic stimulation. **a,** *Left:* Schematic of experimental design. *Right:* Representative

624   wide-field fluorescence image illustrating the robust expression of ChR2-mCherry at the injection site (right BC) and along the CC. Medial

625   is to the left. Red, AAV5.CaMKII.ChR2-mCherry. Scale bar, 1 mm. **b,** Average time courses of fMRI signal changes in right BC (n = 8

626   animals) upon optogenetic stimulation. Error bars represent mean±SD. **c,** Averaged fMRI map showing the strong antidromic activation in

627   BC in the right hemisphere with fiber optic trace (blue arrow) during optogenetic stimulation of CC from 8 rats of block design: 8 s on/ 52 s

628   off, 11 epochs, 10 ms light pulse, 5 Hz. **d,** *Top:* Averaged BOLD signals upon different stimulation frequencies (2 Hz in blue, 5 Hz in red).

629   Error bars represent mean±SD. *Lower:* Mean amplitudes of the BOLD signals (0-10.5 s) for 2 Hz and 5 Hz (n=8, paired t test, *p=0.006).

630   Error bars represent mean±SD. **e**, *Left:* The representative local field potential (LFP) for antidromic activation (gray lines, light pulses). *Right:*

631   Laser power dependent LFPs (pulse width, 10 ms). **f**, Representative BOLD map showing the activity in the projected motor cortex (red

632   arrows) and posterior thalamus (magenta arrow) from the antidromic activity in the BC. Broken boxes showed the enlarged view of projected

633   motor cortex (GLM-based t-statistics in AFNI is used. P (corrected)=0.0319). **g,** Schematic of experimental design. **h,** The representative

20

634   LFP for direct BC light stimulation (blue) and antidromic activation (red) recorded with light pulse durations of 2, 5 and 10 ms. **i,** The

635   different peak latency and transit time for the LFP induced by CC and BC light stimulation (n = 6 animals, paired t test, *p = 0.002, **p =

636   0.009, pulse width, 10 ms). Error bars represent mean±SD.

637

638
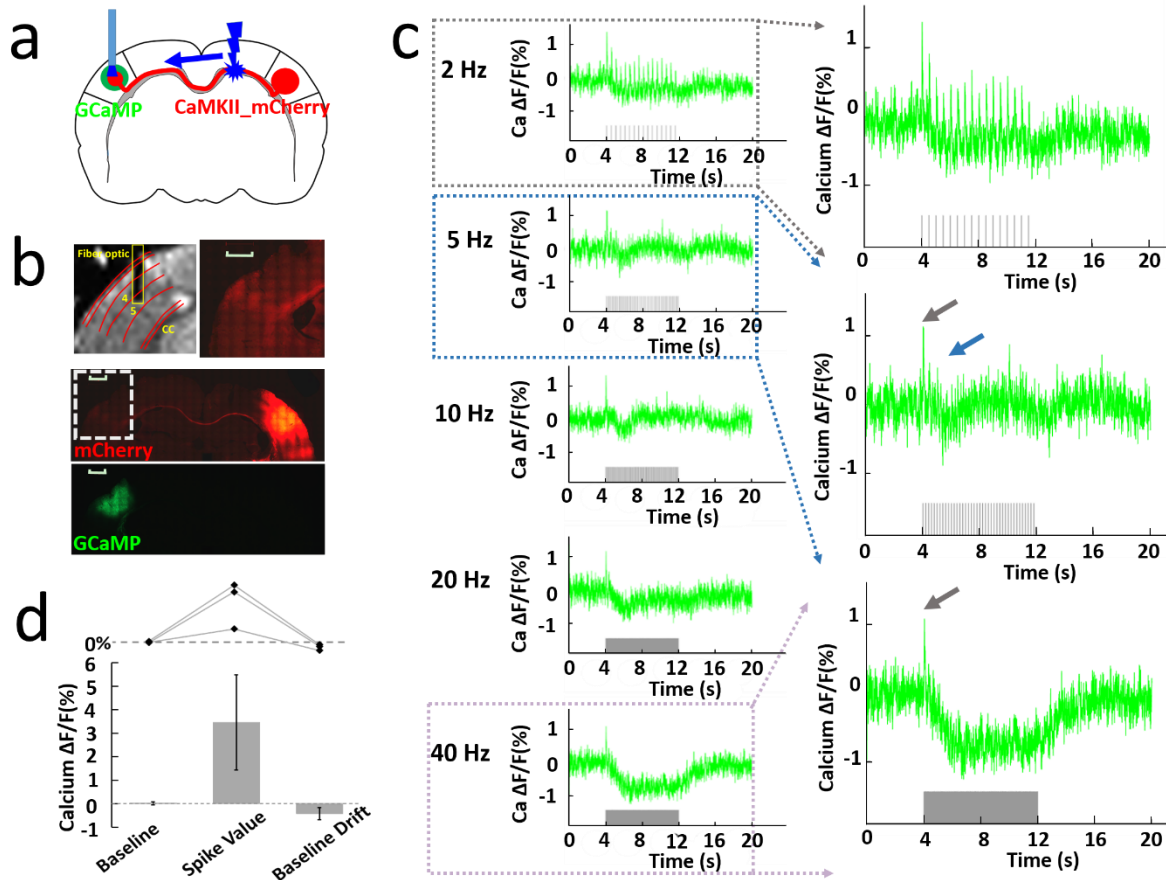
Fig.2. Orthodromic activation upon corpus callosum optogenetic stimulation. **a,** Schematic of experimental design. **b,** *Top left:* Representative RARE anatomical image used to identify the optical fiber location for calcium signal recording in the layer V of barrel cortex. Top right: Enlarged immunostaining image illustrating the ChR2-mCherry expression in the left hemisphere (opposite to the injection site). *Middle:* Representative wide-field fluorescence image illustrating robust ChR2-mCherry at the injection site (right BC) and along the axonal fibers to the other hemisphere. Red, AAV5.CaMKII.ChR2-mCherry. *Bottom:* The immunostaining image illustrating robust GCaMP6f expression (green) in the left barrel cortex. Scale bar, 1 mm. **c,** *Left:* Representative calcium signal changes upon 8 s of orthodromic activation responses to 2, 5, 10, 20 and 40 Hz stimulation. *Right:* Enlarged calcium signal changes responses to 2, 5 and 40 Hz stimulation. **d,** The analysis of calcium baseline, spike value and baseline drift from 3 animals. Error bars represent mean±SD.

647
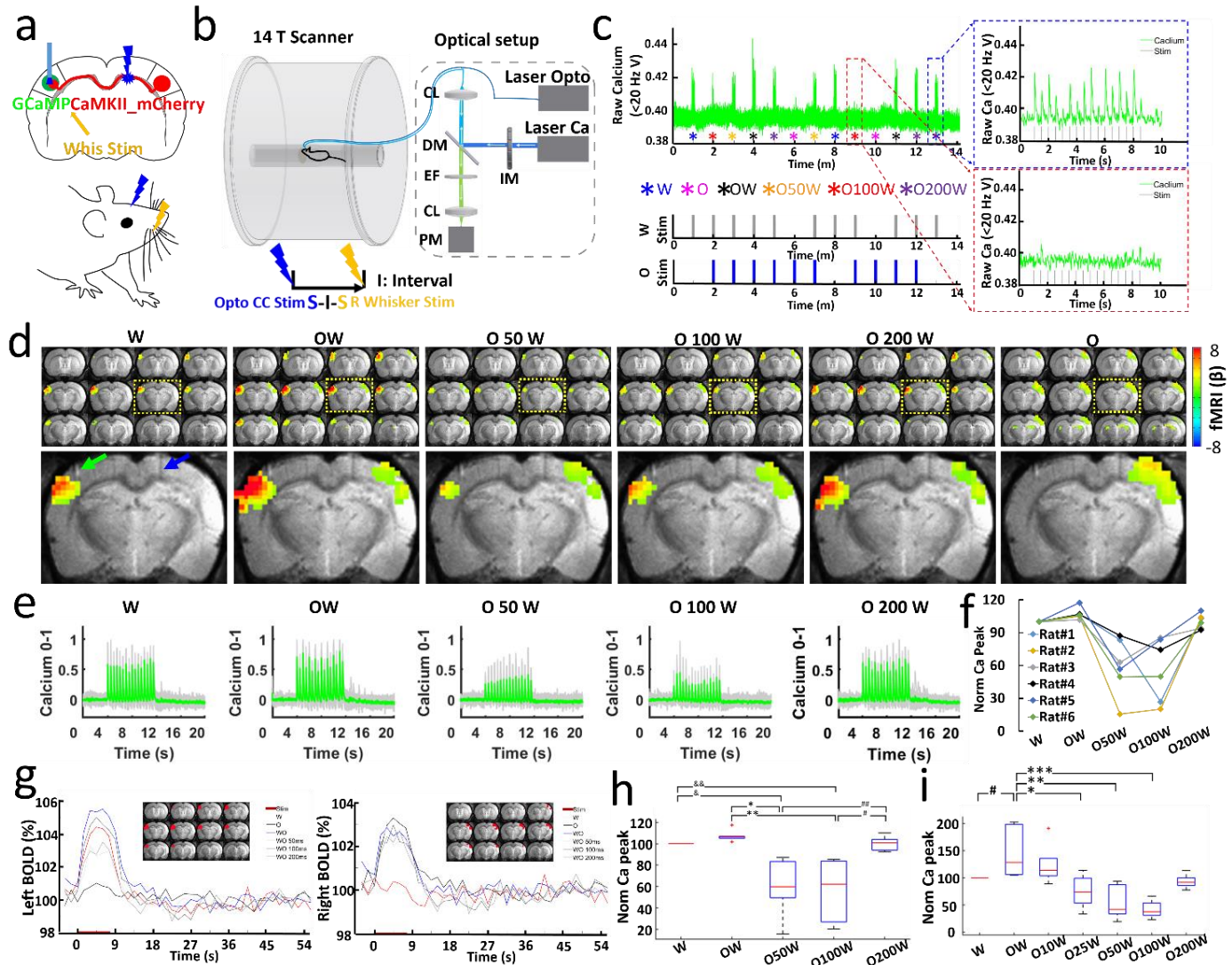
22

Fig. 3. Simultaneous measurement of BOLD and calcium signals during CC optogenetic stimulation and electrical whisker stimulation with varying time intervals. **a,** Stimulation scheme. There are 6 conditions, whisker stimuli only (W), CC stimuli only (O), CC stimuli and whisker stimuli together (OW), CC stimuli and 50 ms, 100ms, 200 ms delayed whisker stimuli (O50W, O100W, O200W). **b,** Schematic drawing of the experimental setup to conduct optogenetic fMRI with simultaneous fiber-optic calcium recording. CL: Coupling Lens, DM: Dichroic Mirror, EF: Emission Filter, PM: Photomultiplier, IM: Intensity Modulation. **c,** Typical calcium signals for condition W (blue dash box) and O100W (red dash box) from a representative rat. **d,** *Top:* Averaged fMRI map of brain-wide activity for 6 conditions across 6 rats (GLM-based t-statistics in AFNI is used). p (corrected) < 0.01 of block design: 8 s on/ 52 s off, 13 epochs, 20 ms light pulse, 2 Hz, 5-39 mw. *Bottom:* Enlarged brain slice showing the differences of BOLD mapping in BC in both hemispheres with fiber optic trace for optogenetic stimulation (blue arrow) and calcium recording fiber (green arrow). **e,** Averaged normalized calcium signal in left BC, grey lines showing the individual normalized calcium signal from 6 rats (Trials # = 29, details see Methods, table 1). **f,** Normalized calcium signal for an individual rat as a function of conditions: W, OW, O50W, O100W, O200W. **g,** *Left:* Averaged BOLD changes in the ROI (red region on anatomical images) in the left BC induced by whisker stimulation. *Right:* averaged BOLD changes in the ROI (red region on anatomical images) in the right BC induced by CC stimulation. **h,** Averaged normalized calcium signal changes across 6 rats modulated by stimulus time intervals (ANOVA, p < 0.01). **i,** Averaged normalized calcium signal changes across 4 rats modulated by stimulus time intervals (ANOVA, p < 0.03).
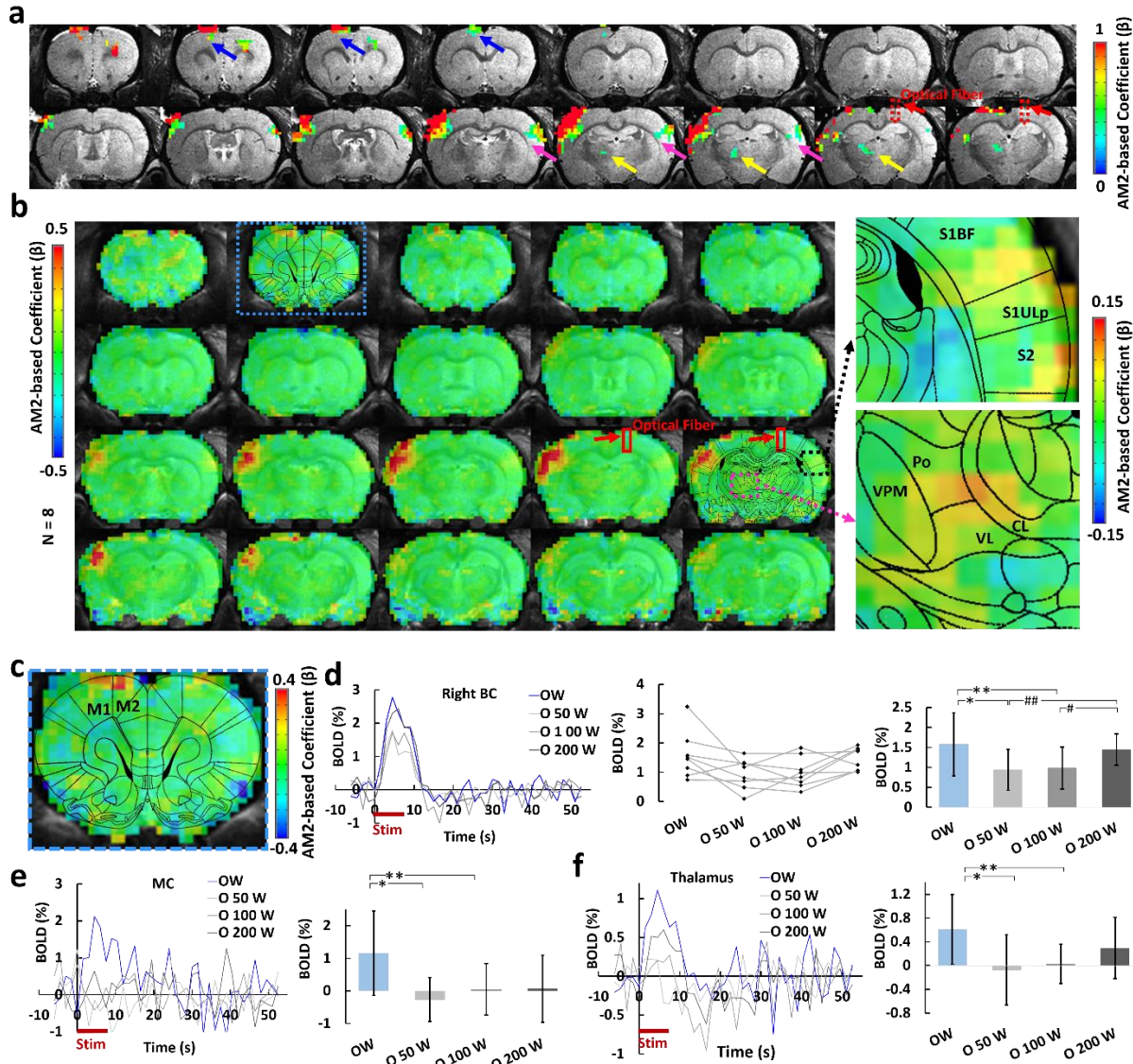
Fig. 4. Calcium AM-based whole brain BOLD correlation analysis. **a**, one representative animal map overlaid on the anatomical image with a statistical threshold (p (corrected) < 0.05, cluster size > 15 voxels, MC, blue arrows, BC, magenta arrows, PO, yellow arros, optical fiber trace, red arrows). **b**, Group-averaged correlation maps show the spatial distribution of the positive correlation located at left BC, MC, as well as the PO by overlying with the brain atlas (red square, optical fiber traces, right panel: the enlarged images of the correlation map overlaid on the brain atlas). **c**, Enlarged correlation map shows the positive correlation at the MC. **d**, *Left*: Averaged time courses from the right BC at different conditions (n = 8 rats). *middle*: Mean amplitudes of the BOLD signals (0-10.5 s) for individual rats. *Right*: Averaged amplitudes of the BOLD signals (0-10.5 s, mean±SD, ANOVA, *p = 0.027, **p = 0.004, #p = 0.030, ##p = 0.003). **e**, *Left:* averaged time courses from the MC (n = 8 rats). *Right:* Averaged amplitudes of the BOLD signals (0-10.5 s, mean±SD, ANOVA, *p = 0.005, **p = 0.01). **f**, *Left:* Averaged time courses from the PO (n = 8 rats). *Right*: Averaged amplitudes of the BOLD signal (0-10.5 s, mean±SD, ANOVA, *p = 0.009, **p = 0.012). W: whisker stimulation only, OW: simultaneous optical and whisker stimulation, O[x]W optical stimulation followed by [x] ms-delayed whisker stimulation.

24

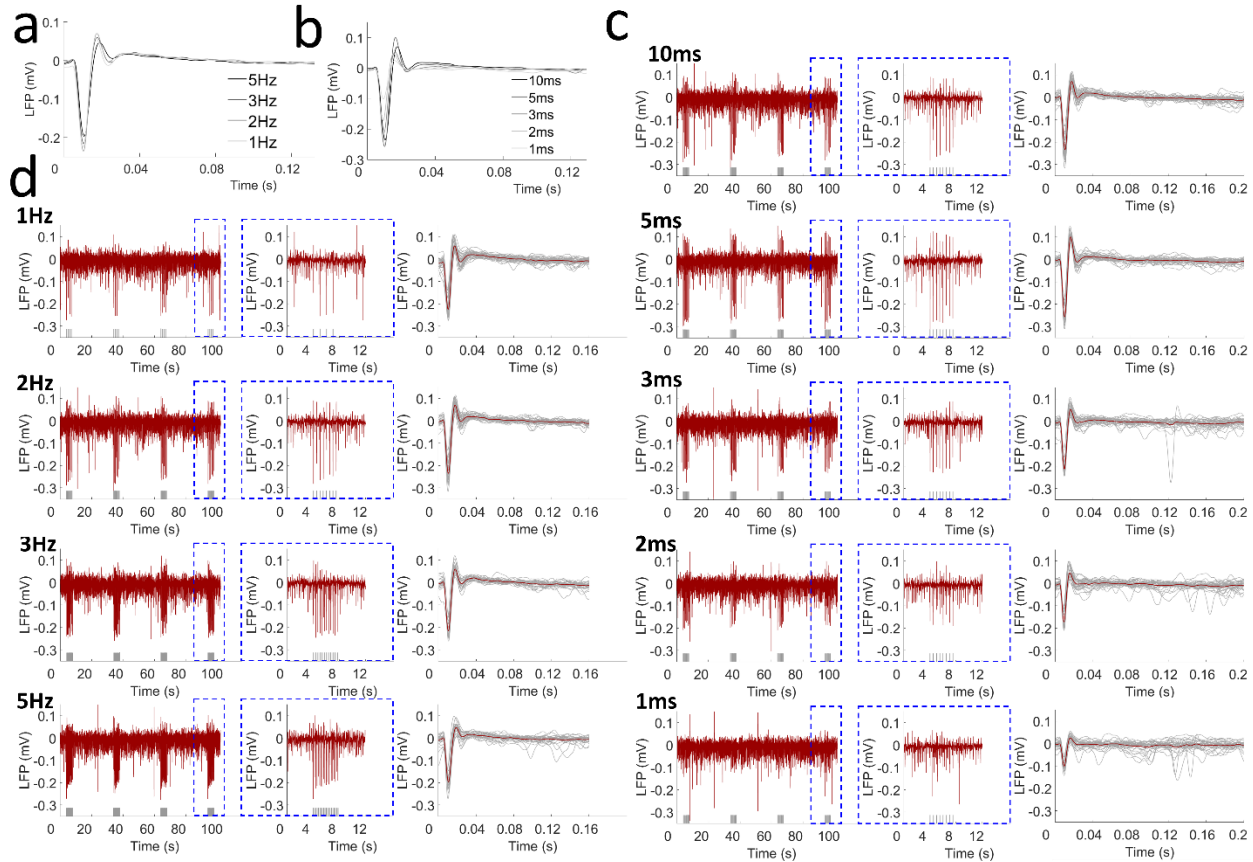# Supplementary information
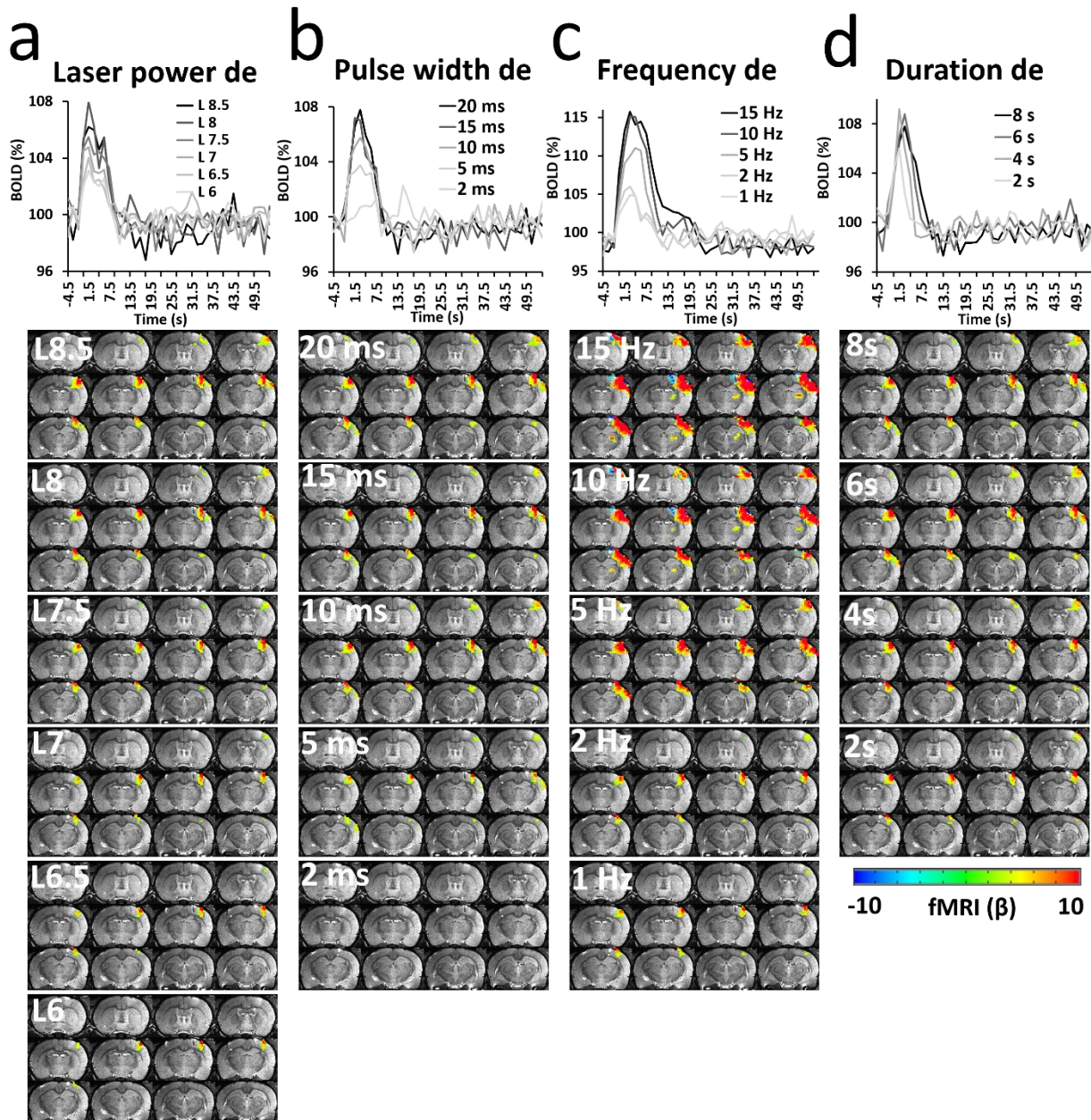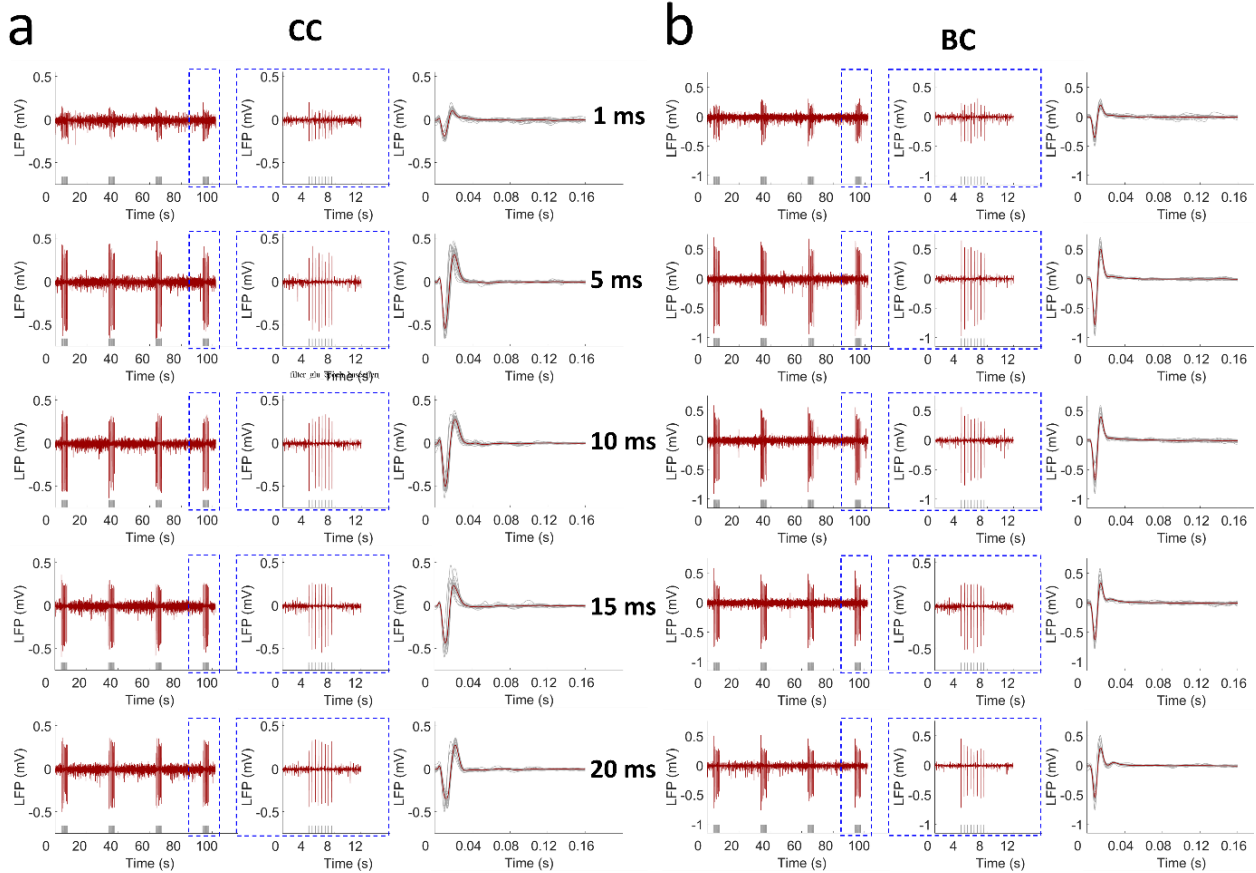

Supplementary Figure 1. Representative functional maps and time courses of the fMRI signal (average of 13 epochs, 60 s per epoch) upon CC light activation with (**a**) laser power dependency (2 Hz, 8 s, 20 ms pulse width), (**b**) pulse width dependency (2, 5, 10, 15 and 20 ms pulse width, 2 Hz, 8 s, L 8), (**c**) frequency dependency (1, 2, 5, 10 and 15 Hz, 8 s, L 8, 20 ms pulse width) and (**d**) duration dependency (2, 4, 6 and 8 s, 2 Hz, 20 ms pulse width, L 8). It is noteworthy that exposure to light with high frequency (10 and 15 Hz) at high power (35 mW) led to heating effects, inducing artifacts close to the fiber tip (**c**), as well as very strong antidromic activity. GLM-based t-statistics in AFNI is used, p (corrected) < 0.005.

Supplementary Figure 2. The light-driven antidromic LFP with frequency and pulse width dependency of a representative rat. (**a**) Averaged LFP driven by light pulses at different frequencies (1, 2, 3 and 5 Hz; 10 ms pulse width, L 7.5, 4 s stimulation 26 s rest, 16 epochs). (**b**) Averaged LFP driven by light pulses at different pulse widths (1, 2, 3, 5 and 10 ms pulse width; 2 Hz, L 7.5, 4 s stimulation 26 s rest, 16 epochs). (**c**) The raw LFP trace by optogenetic stimulation (*left*, 4 epochs), the enlarged representative LFP for one epoch (*middle*) and the averaged LFP from one trial (red line).The grey lines show all the LFP from this trial (*right*) upon different stimulation frequencies. (**d**) The raw LFP trace during optogenetic stimulation (*left*, 4 epochs), the enlarged representative LFP for one epoch (*middle*) and the averaged LFP from one trial (red line). The grey lines show all the LFP from this trial (*right*) upon different stimulation light pulse widths. Grey lines beneath the LFP indicate the stimulation.
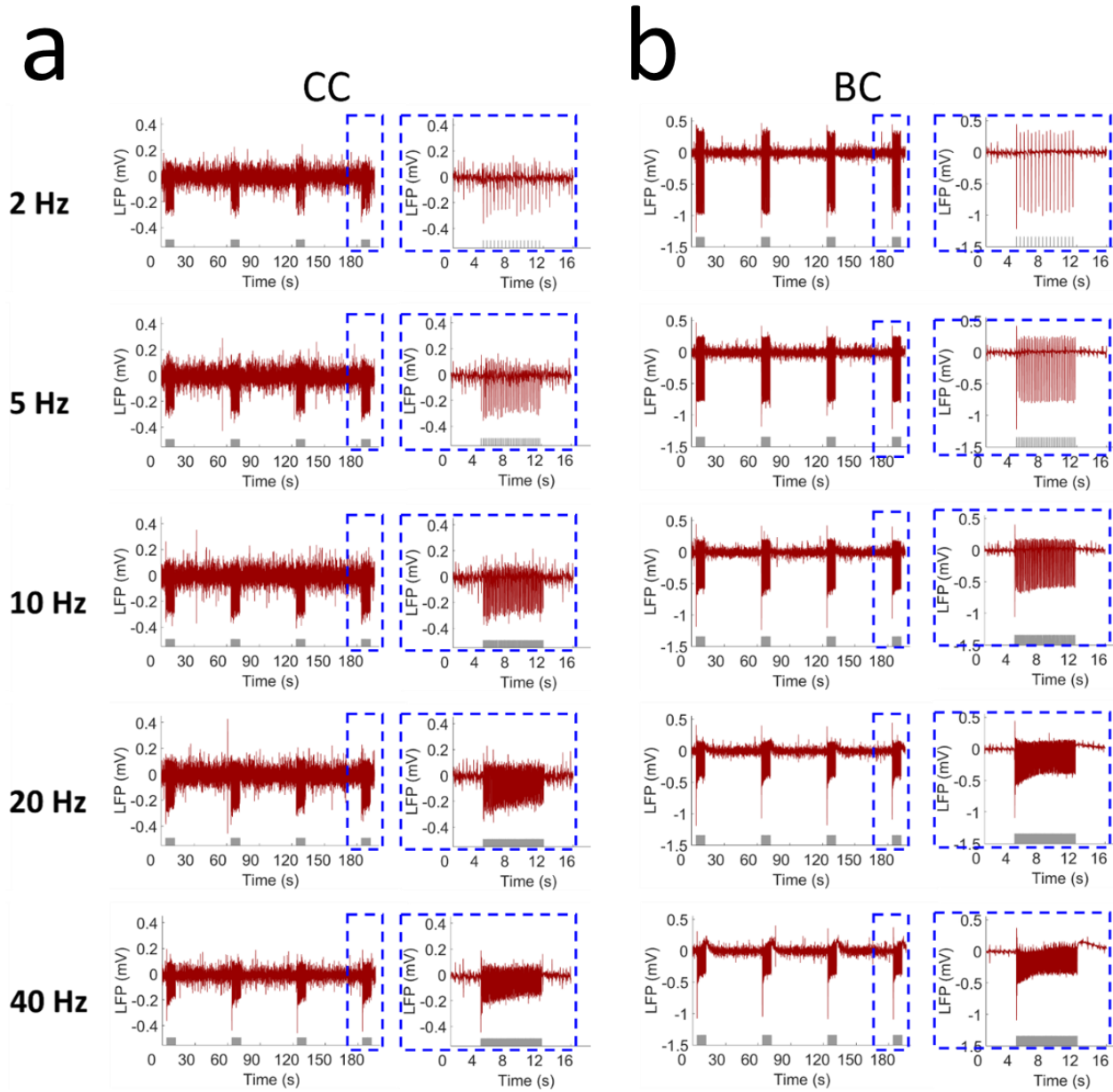
694

Supplementary Figure 3. Light-driven LFP for antidromic activity from CC (**a**) stimulation and BC (**b**) direct stimulation showing similiar pattern with pulse width dependency of a representative rat. Every panel in **a** and **b** shows the raw LFP trace observed upon optogenetic stimulation (*left*, 4 epochs), the enlarged representative LFP for one epoch (*middle*) from the dashed blue box and the averaged LFP from one trial (red line). The grey lines show all the LFP from this trial (*right*). Grey lines beneath the LFP indicate the stimulation.
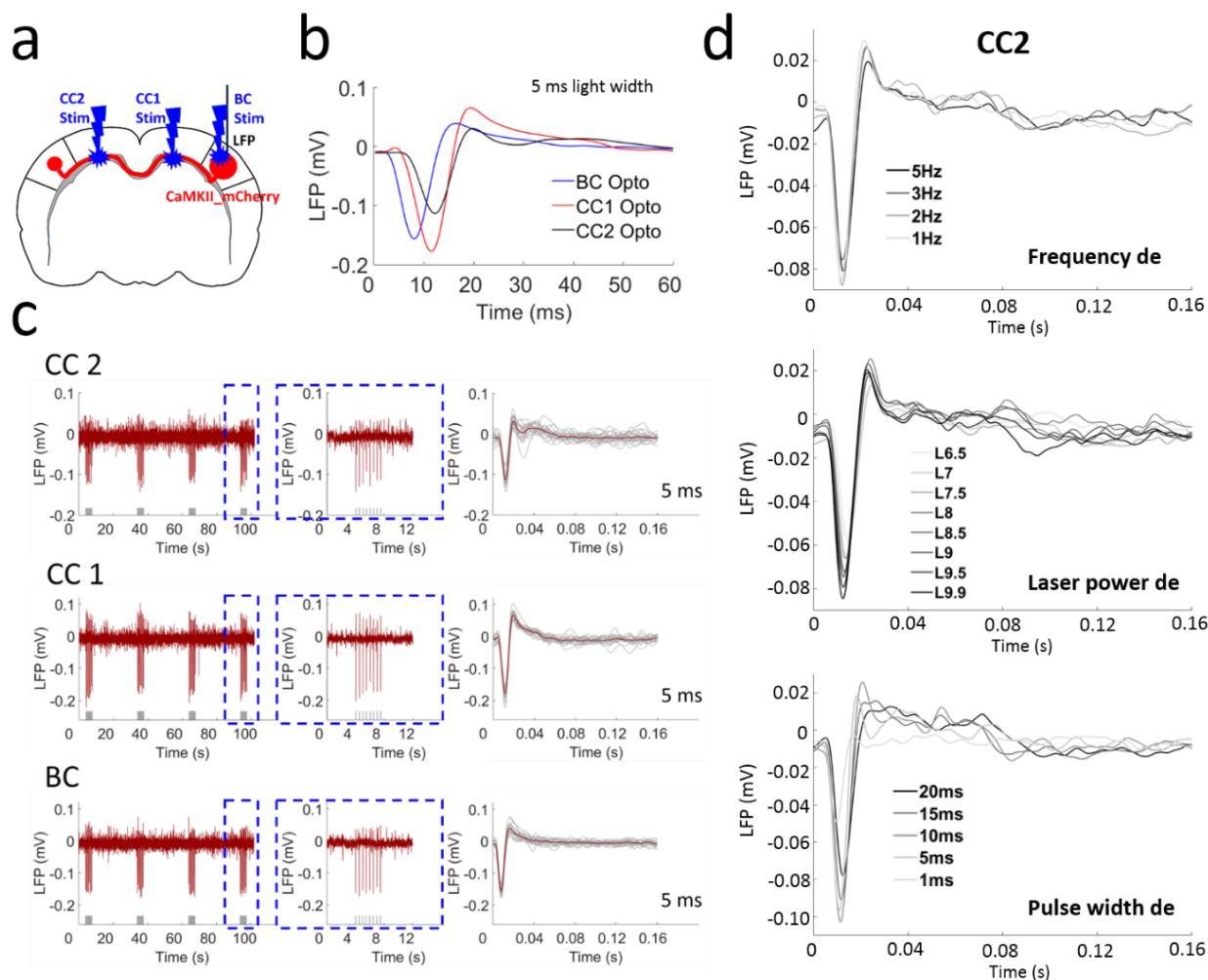
700

Supplementary Figure 4. Light-driven LFP for antidromic activity from CC stimulation (**a**) and BC direct stimulation (**b**) showing similar pattern with frequency dependency of a representative rat. Every panel in **a** and **b** shows the raw LFP trace by optogenetic stimulation (*left*, 4 epochs), the enlarged representative LFP for one epoch (*right*) from the dashed blue box. Grey lines beneath the LFP indicate the stimulation.
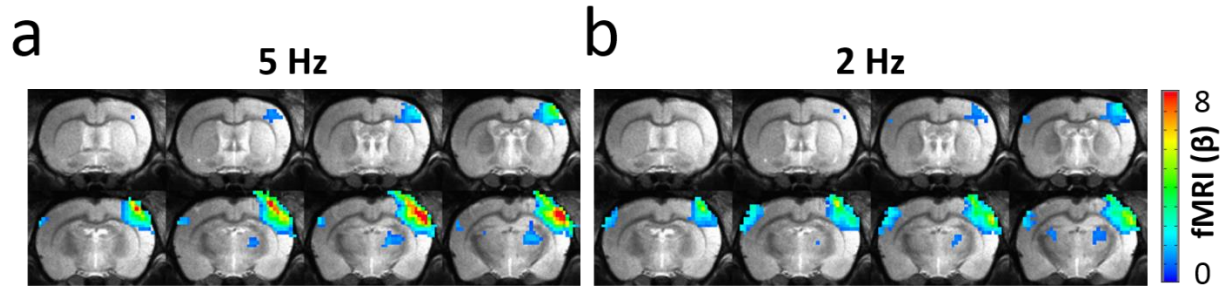
Supplementary Figure 5. Light-driven LFP for antidromic activity from CC stimulation in both hemispheres and BC direct stimulation. (**a**) The schematic plan for the experiment design. (**b**) Averaged LFP from the CC2 stimulation in the hemisphere opposite to the virus injection site (blue line), CC1 stimulation in the same hemisphere (red line) and BC direct stimulation (black line) shown different temporal features. (**c**) The raw LFP trace by optogenetic stimulation (*left*, 4 epochs), the enlarged representative LFP for one epoch (*middle*) from the dashed blue box and the averaged LFP from one trial (red line). The grey lines show all the LFP from this trial (*right*). (**d**) Averaged LFP upon optogenetic stimulation of CC2 with frequency (*upper panel*), laser power (*middle panel*) and pulse width (*lower panel*) dependency showing reliably detected antidromic activity.

716

Supplementary Figure 6. Light-driven functional maps demonstrating opposite relationships for antidromic and orthodromic activities in the BC to 5 Hz (a) and 2 Hz (b). The antidromic activity in the right hemisphere and the orthodromic activity in the left hemisphere responses to 5 Hz was stronger and weaker, respectively, compared to 2 Hz. GLM-based t-statistics in AFNI is used. p (corrected) < 0.01.
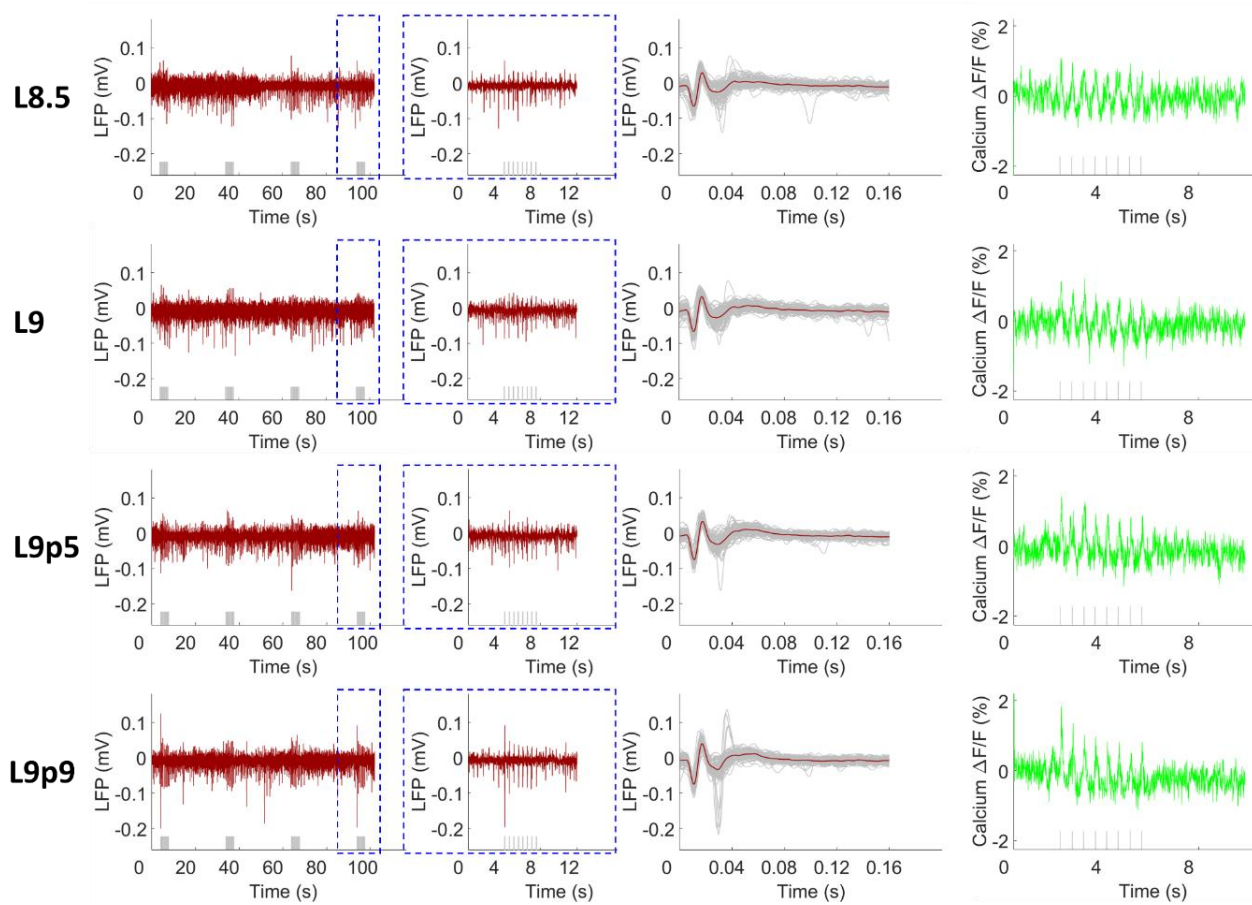
721

Frequency dependency
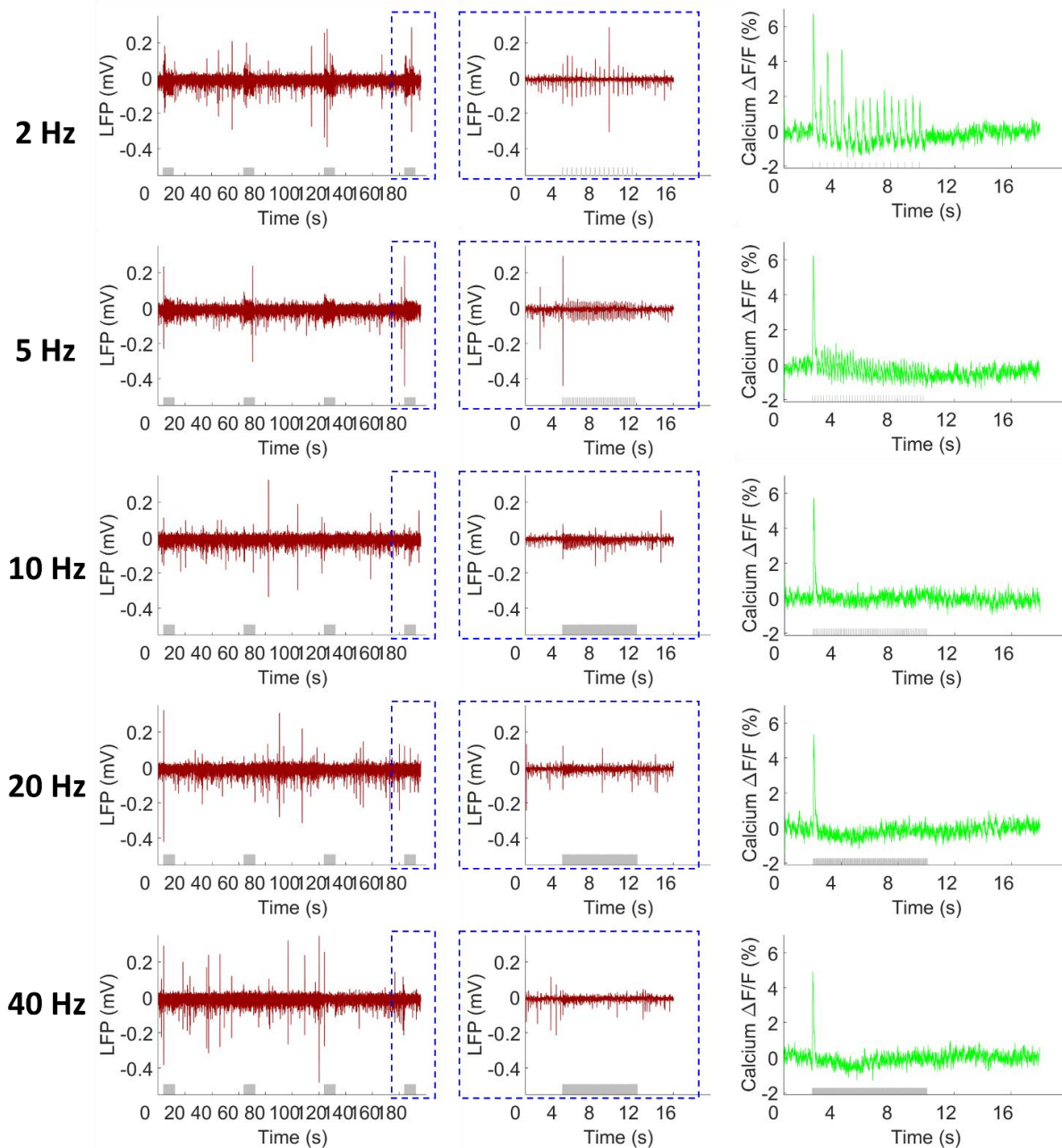
Supplementary Figure 7. The frequency dependency of simultaneous LFP (red) and calcium response signals (green). Every panel shows the raw LFP trace elicited by optogenetic stimulation (*left*, 4 epochs), the enlarged representative LFP for one epoch from the dashed blue box (*middle*) and averaged calcium signal (8 s stimulation 52 s rest, 15 epochs, L9, pulse width 10 ms). Grey lines beneath the LFP and calcium signals indicate the stimulation.

Laser power dependency

Supplementary Figure 8. The laser power dependency of simultaneous LFP (red) and calcium signals (green) showing that both amplitudes increased as a function of the laser power. Every panel shows the raw LFP trace elicited by optogenetic stimulation (*left*, 4 epochs), the enlarged representative LFP for one epoch from the dashed blue box (*middle*), the averaged LFP from one trial (red line). Grey lines showing all the LFP from this trial (*right*) and the averaged calcium signal (4 s stimulation 26 s rest, 11 epochs, L9, pulse width 10 ms). Grey lines beneath the LFP and calcium signals indicate the stimulation.
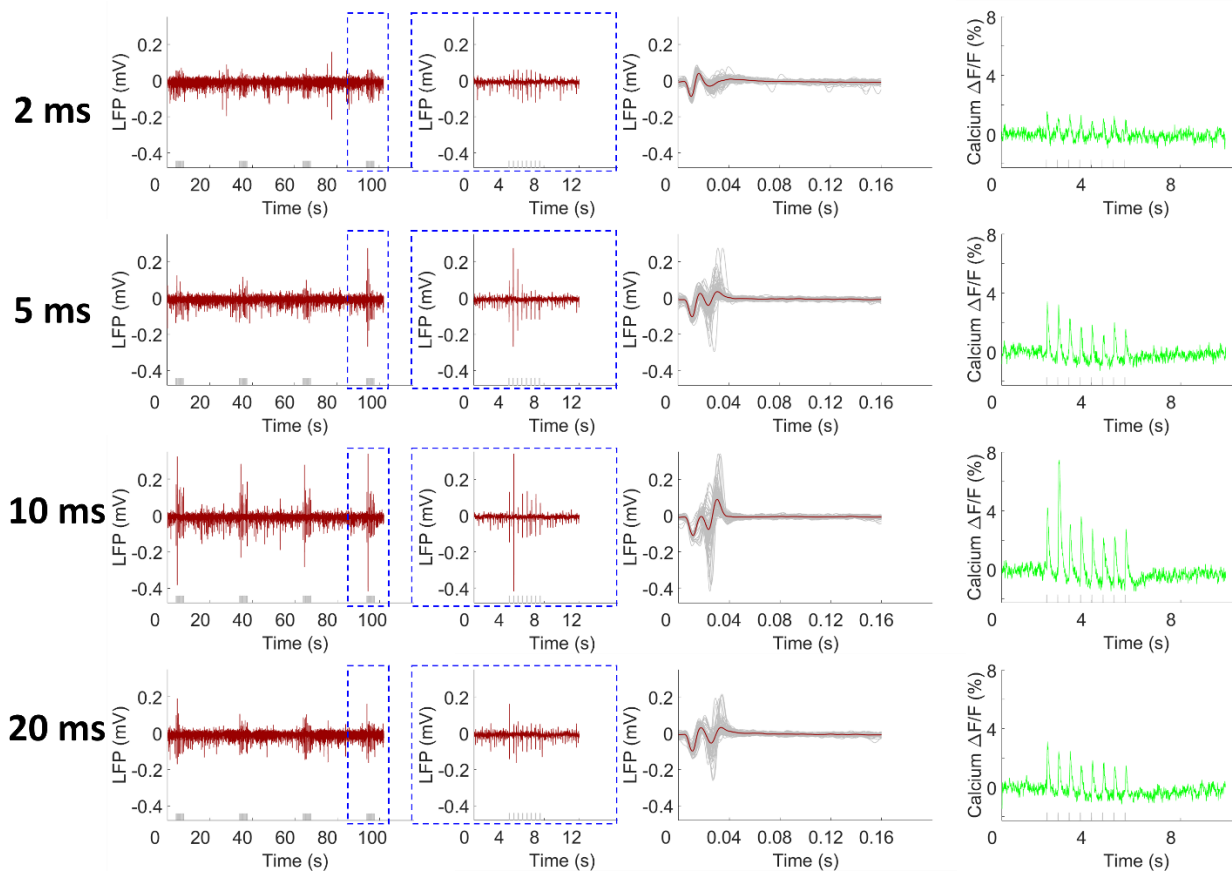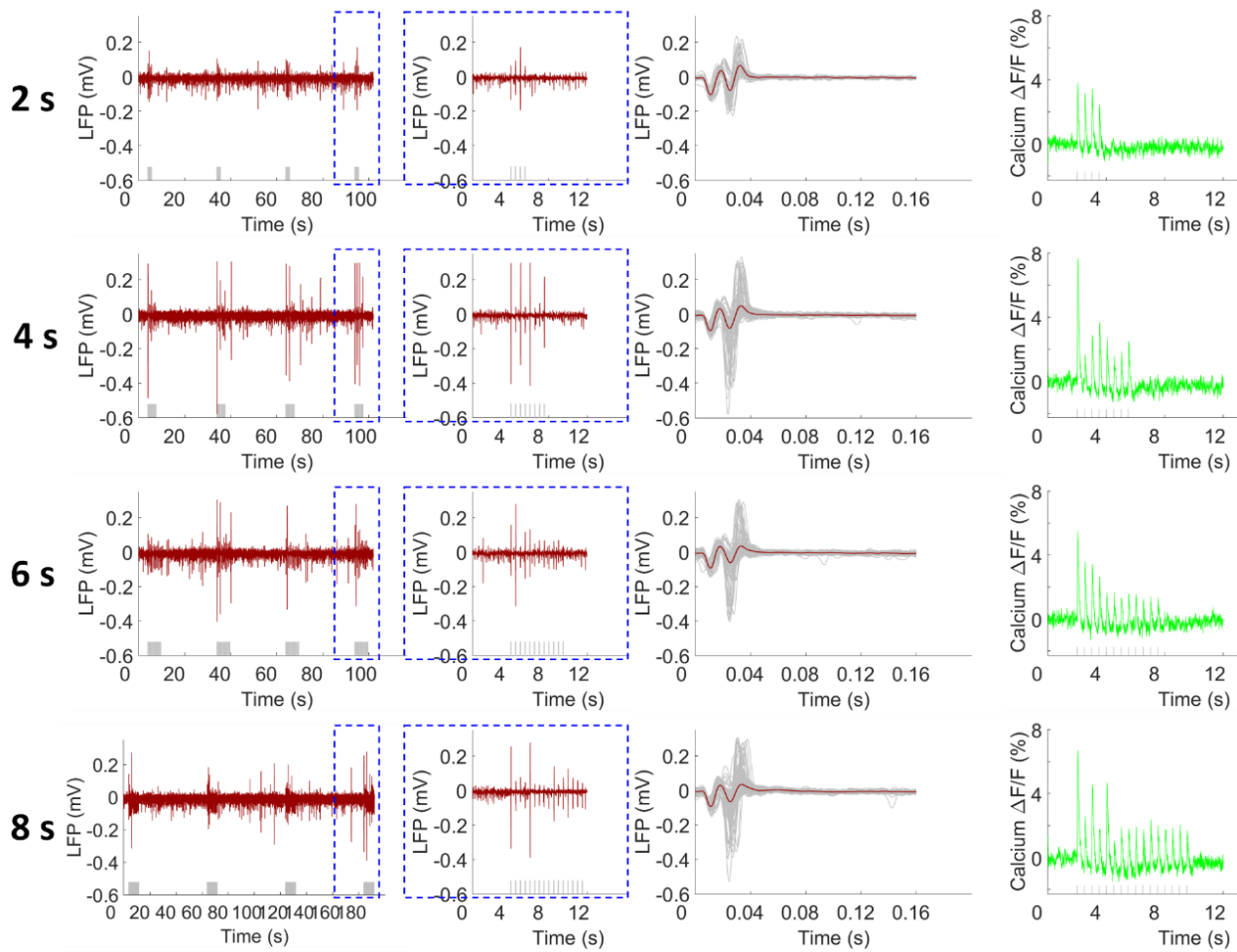
Laser pulse width dependency

Supplementary Figure 9. The laser pulse width dependency of simultaneous LFP (red) and calcium signals (green). Calcium signals increased and the LFP pattern demonstrated stronger depolarization according to the increased pulse width at 2 ms, 5 ms and 10 ms. In contrast, for the 20 ms pulse width stimulation, there was decreased calcium signal and weaker depolarization of LFP. Every panel shows the raw LFP trace elicited by optogenetic stimulation (*left*, 4 epochs), the enlarged representative LFP for one epoch from the dashed blue box (*middle*), the averaged LFP from one trial (red line, with the grey lines showing all the LFP from this trial) (*right*) and the averaged calcium signal (2 Hz, 4 s stimulation 26 s rest, 11 epochs, L9). Grey lines beneath the LFP and calcium signals indicate the stimulation.

## Duration dependency


Supplementary Figure 10. The duration dependency of simultaneous LFP (red) and calcium signals (green). Every panel shows the raw LFP trace elicited by optogenetic stimulation (*left*, 4 epochs), the enlarged representative LFP for one epoch from the dashed blue box (*middle*), the averaged LFP from one trial (red line, with the grey lines showing all the LFP from this trial) (*right*) and the averaged calcium signal (2 Hz, 11 epochs, L9, pulse width 10 ms). Grey lines beneath the LFP and calcium signals indicate the stimulation.

750
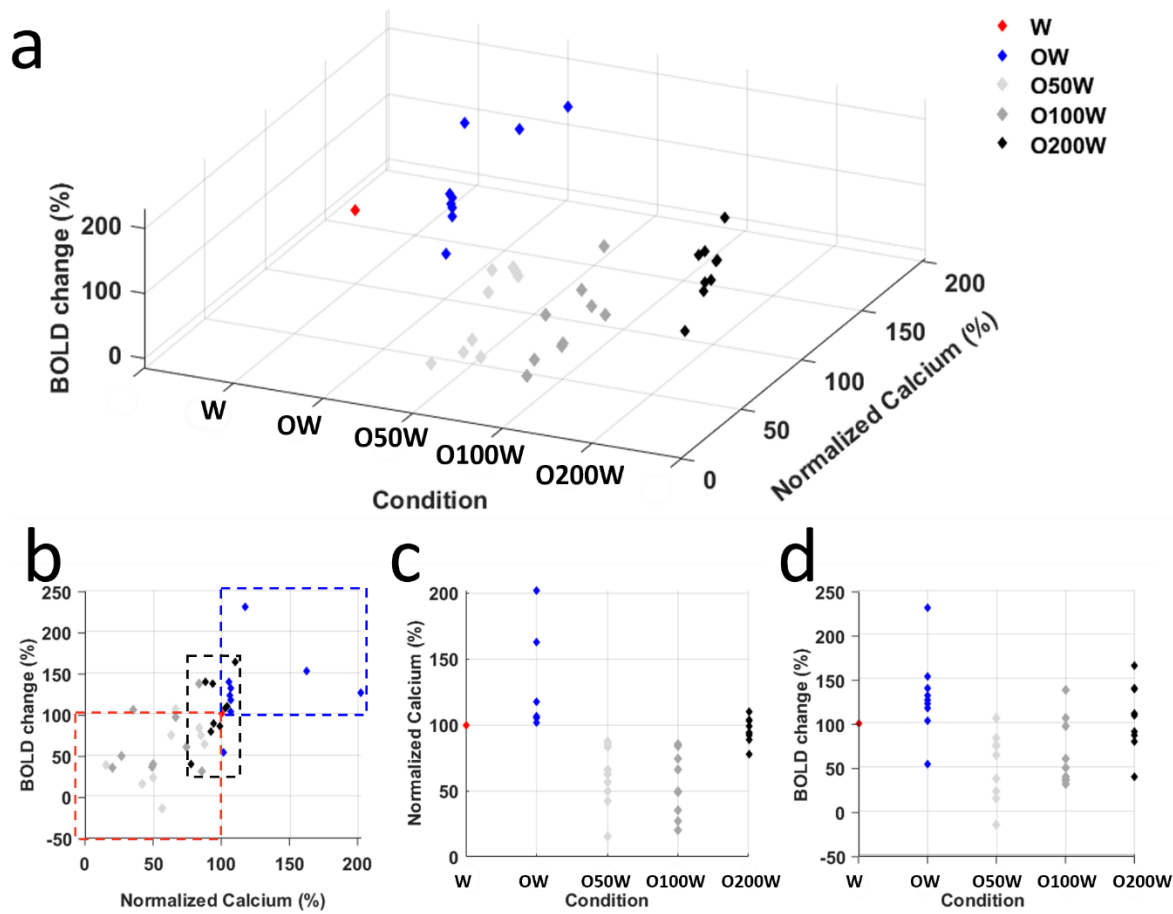
Supplementary Figure 11. The scatter plots of the evoked BOLD and calcium signals for 5 stimulation conditions (W, OW, O50W, O100W and O200W) in 9 animals. (**a**) 3D plot of the BOLD changes (Z axis), calcium changes (Y axis) and stimulation conditions (X axis). Both BOLD and calcium signals are normalized to condition W. (**b**) View from the correlation of BOLD changes with calcium signals. The central red diamond is the baseline to which the data were normalized. Blue diamonds represent the condition OW, most of them distributed in the dashed blue box, showing increased neuronal activities. Light grey diamonds and dark grey diamonds represent the condition O50W and O100W, respectively, most of them located in the dashed red box, showing suppressed neuronal activities. (**c**) Normalized calcium signals as a function of condition. (**d**) Normalized BOLD changes as a function of condition. W: whisker stimulation only, OW: simultaneous optical and whisker stimulation, O[x]W optical stimulation followed by [x] ms-delayed whisker stimulation.
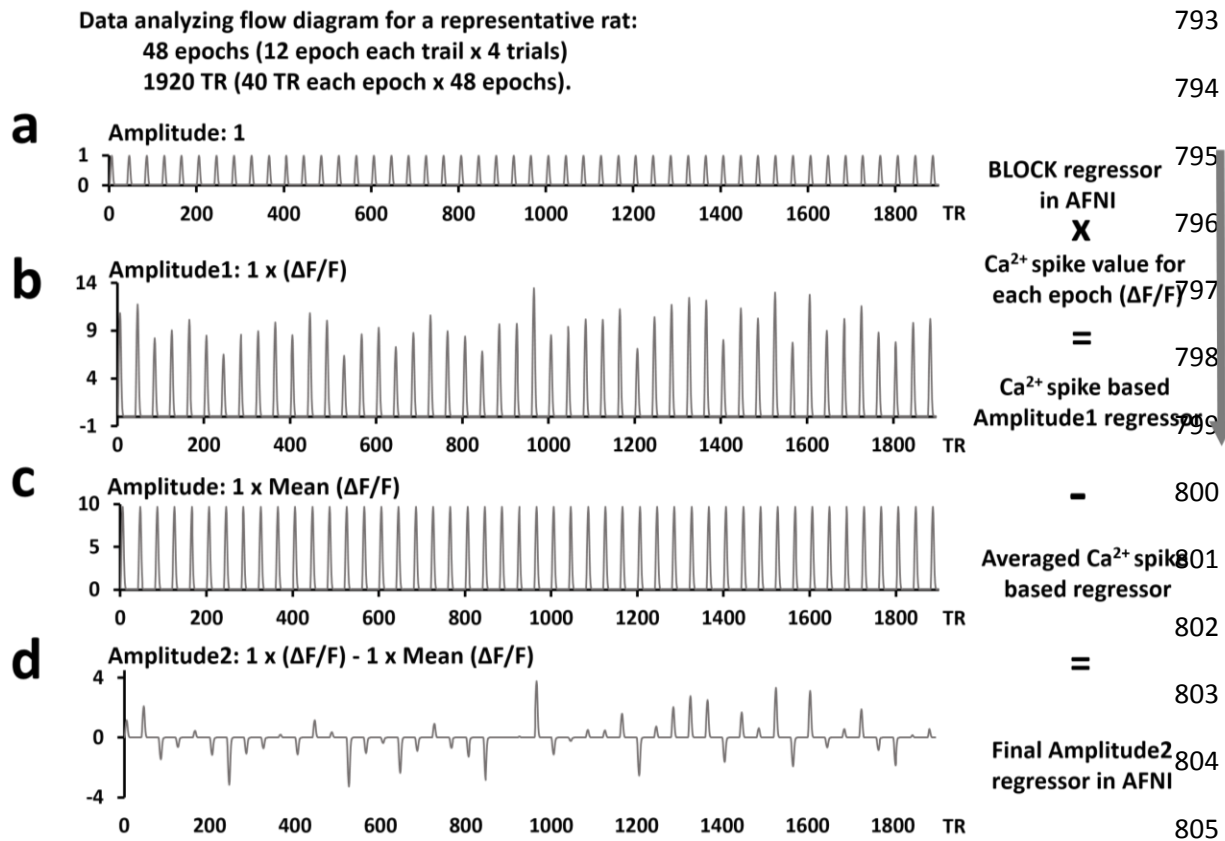
760
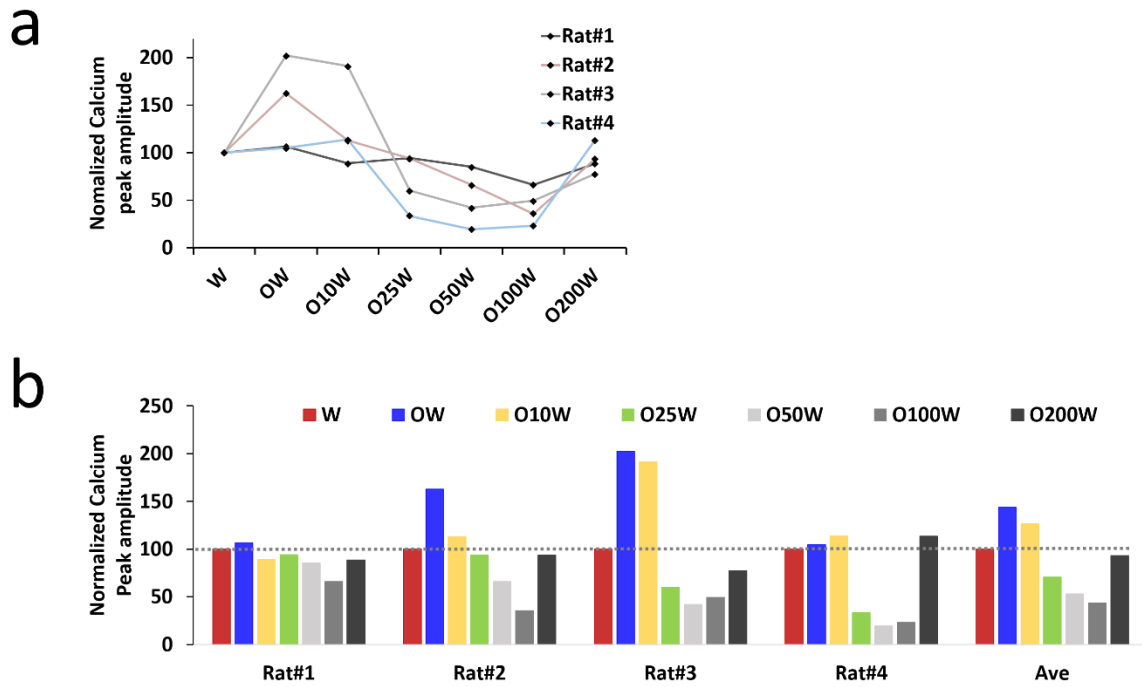
Supplementary Figure 12. The effect of conditioning stimuli in the sensory evoked calcium signals in the left hemisphere for 7 refined conditions (W, OW, O10W, O25W, O50W, O100W and O200W). (**a**) The scatter plot of the calcium signals normalized to condition W from 4 rats. (**b**) The individual pattern changes of calcium signals from 4 animals, as well as the averaged calcium signal change pattern for all the 7 conditions.
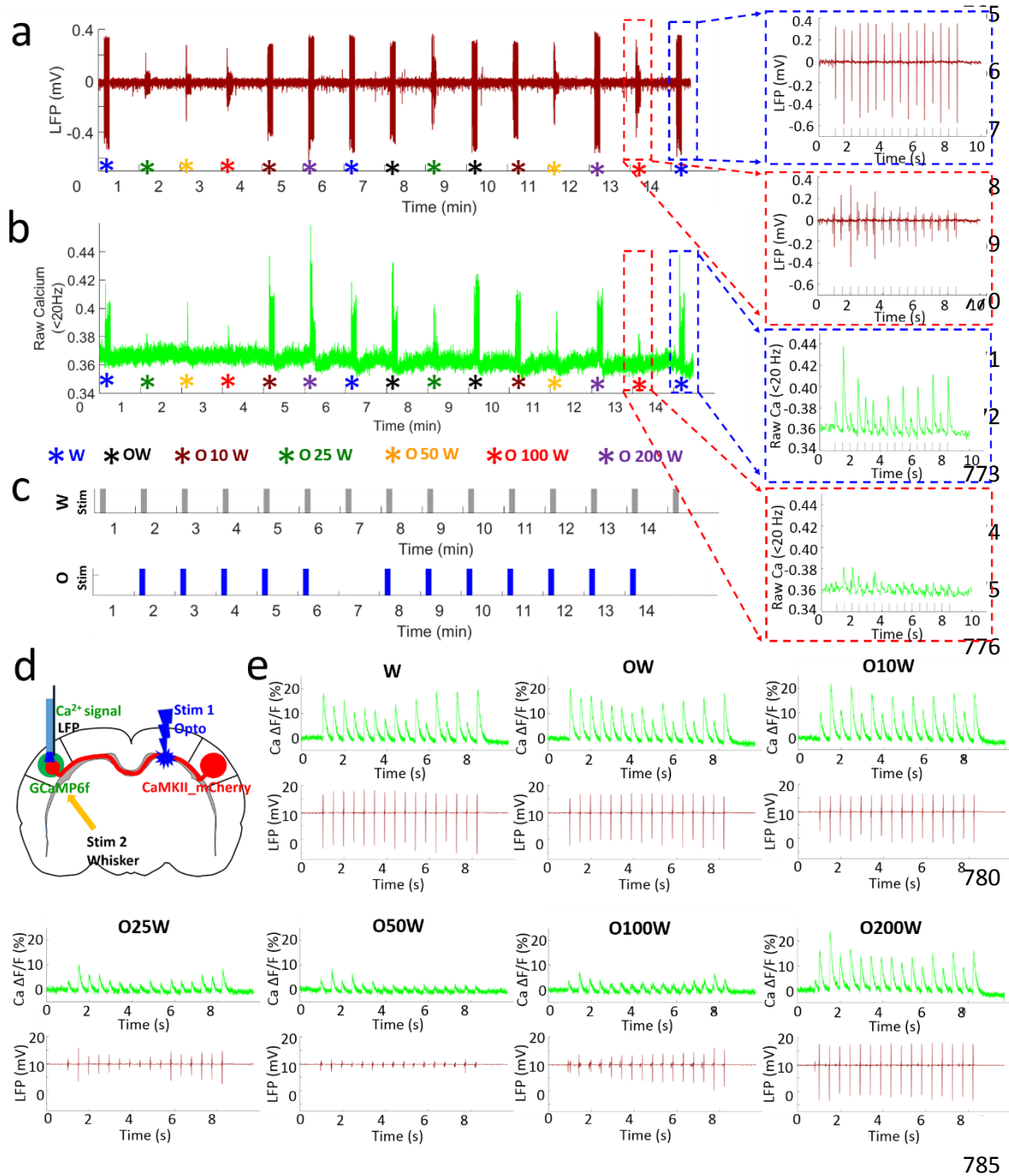
Supplementary Figure 13. Typical LFP (red) and calcium signals (green) of one trial from a representative rat. (**a**) Different amplitudes of LFP and (**b**) calcium signal changes showing the different neuronal activity upon seven randomized stimulation conditions. (**c**). Simplified diagram representing the typical calcium signals and LFP for condition W (blue dash boxes in **a** and **b**, upper graph in **c**) and O100W (red dash boxes in **a** and **b**, lower graph in **c**) in one epoch. (**d**) Schematic of the experimental design. (**e**) Averaged calcium signals and LFP in left barrel cortex, further confirming the spatial and temporal features of sensory-evoked cortical activity pattern shaped by callosal inputs. W: whisker stimulation only, OW: simultaneous optical and whisker stimulation, O[x]W optical stimulation followed by [x] ms-delayed whisker stimulation.

Data analyzing flow diagram for a representative rat:
48 epochs (12 epoch each trail x 4 trials)
1920 TR (40 TR each epoch x 48 epochs).

806 **Supplementary Figure 14.** The flow diagram to generate the calcium signal-based regressor for the fMRI correlation map.
807 (**a**), version 1 of the regressor, generated with the parameter BLOCK (L, 1), which generates a convolution of a square wave
808 of duration L with the stimulation train and makes a peak amplitude of block response = 1. (**b**), the variable calcium amplitude
809 of each epoch from a representative rat is used to generate the AM1 (amplitude modulated 1) regressor in 3dDeconvolve
810 command in AFNI. (**c**), the averaged calcium amplitude of all the epochs is used to generate the regressor of no interest. (**d**),
811 by computing 'b – c', the differences from the mean calcium amplitude can be detected. This new vector constitutes the final
812 regressorAM2. 'AM2' allows to detect voxels that activate but do not change proportionally to the amplitude factor, as well as
813 provides a direct measure of the proportionality of the activation in response to changes in the input amplitude factors (from
814 the description of 3dDeconvolve program in AFNI).

815